Satellite-based Assessment of Continuous and Episodic Flaring Regimes across Major Oil and Gas-producing Basins

Lulu Si[1,*], Shanyu Zhou[1], Debbie Walker[2], Itziar Irakulis-Loitxate[2], Javier Gorroño[1], Mark F. Lunt[3], and Luis Guanter[1]

[1]Research Institute of Water and Environmental Engineering (IIAMA), Universitat Politècnica de València (UPV), 46022. Valencia, Spain.
[2]International Methane Emission Observatory (IMEO), United Nations Environment Programme, 75015. Paris, France.
[3]Environmental Defense Fund, Perth, WA, Australia

*Email: lsi@doctor.upv.es

This is a non-peer-reviewed preprint submitted to EarthArXiv, submitted to peer review at Environmental Science & Technology.

Abstract

Gas flaring wastes valuable natural gas while emitting large amounts of harmful air pollutants; however, existing flare inventories rarely distinguish the operational behavior across various basins and fuel types, namely oil- and gas-associated flaring.This limits their value for targeted mitigation efforts. Here, we present a satellite-based classification framework for characterizing flaring behavior by combining coarse resolution Visible Infrared Imaging Radiometer Suite (VIIRS) Nightfire (VNF) products with high-spatial resolution Sentinel-2 and Landsat 8/9 imagery. The framework quantifies temporal persistence and identifies operational interruptions from daily VIIRS thermal records, while using Sentinel-2 and Landsat 8/9 imagery to characterize flare site conditions at higher spatial resolution. It then assigns fuel type as oil or gas, yielding four operational categories: continuous oil/gas and episodic oil/gas. Applied to Algeria, Iran, Mexico, Nigeria, Saudi Arabia, and Turkmenistan, the framework identified 1,910 confirmed flare sites, approximately 1.8 times the number detected by VIIRS alone. Our analysis shows that continuous oil flares are the largest category, with 728 sites representing 56% of the classified inventory. Iran has the largest number of continuous oil flares (262) and a more geographically concentrated pattern. Gas flares account for 25% of the classified sites and form the majority of the classified flares in Turkmenistan. These sites were then linked to the gas pipeline infrastructure and compared with multi-scale methane observations. The analysis shows that Iran and Algeria contain the largest flare volumes near gas pipelines, whereas Mexico has a more spatially concentrated recovery opportunity close to existing infrastructure. Oil flares, particularly continuous oil flares, are more frequently co-located with methane plumes in Algeria and Iran than in other countries. Although Saudi Arabia has a high flare count, it has no matched methane plumes. These results reveal systematic differences in the proximity of the infrastructure and the detectability of methane, providing a transferable basis for mitigation prioritization and source attribution.

Keywords

Oil&Gas flaring; VIIRS Nightfire; Sentinel-2; Landsat 8/9; flare classification; methane emissions; mitigation prioritization

1 Introduction

Flaring usually refers to the controlled combustion of petroleum gas at upstream oil and gas (O&G) production facilities. Practiced for over 160 years, it remains a major source of greenhouse gas (GHG) emissions from the energy sector. Complete combustion converts gas to CO_2 and forms nitrogen oxides (NO_x) at high flame temperatures. Incomplete combustion leaves some CH_4 unburned and emits CO, black carbon, and volatile organic compounds (VOCs), while unlit flares release CH_4 directly into the atmosphere [1–7]. With a Global Warming Potential (GWP) of 82.5 over 20 years and 29.8 over 100 years [8, 9], methane gives incomplete flare combustion a disproportionate short-term climate impact. Beyond climate forcing, co-emitted pollutants pose direct public health consequences [10], increased community exposure to air toxics and VOCs [4], and measurable occupational radiation and chemical doses in production facilities [11]. Since 2015, the World Bank's Zero Routine Flaring by 2030 (ZRF) initiative has committed governments and oil companies to end routine flaring [12]. In 2023, the Global Flaring and Methane Reduction (GFMR) Partnership was established to support governments and industry in reducing flaring and methane emissions. ZRF endorsers, representing approximately 60% of the global flaring, have demonstrated measurably better performance than non-endorsing countries. Despite these efforts, global flaring volume reached its highest level since 2007 in 2024 (151 billion cubic meters, bcm). This released an estimated 389 $MMtCO_2e$, including 46 $MMtCO_2e$ from unburnt methane [13]. The top nine flaring countries accounted for approximately three-quarters of all global flaring despite producing less than half of the global oil output. The gas flared annually is equivalent to Africa's total annual gas consumption [13]. However, aggregate flaring continues to rise, underscoring the persistent gap between policy ambition and operational reality [14].

Satellite remote sensing has become the primary tool for monitoring flares on a global scale. The Visible Infrared Imaging Radiometer Suite (VIIRS) Nightfire (VNF) product identifies sub-pixel thermal anomalies during nighttime overpasses of the Suomi-NPP, NOAA-20, and NOAA-21 satellites, providing daily global coverage at an approximate ground sampling distance (GSD) of 750 m [15, 16]. VIIRS-derived products have enabled the systematic mapping of flaring locations and volumetric estimates calibrated against national reporting data [17]. These products form the empirical basis for annual flare volume assessment, though, the 750 m pixel footprint imposes a fundamental detection limit in regions with dense or clustered upstream infrastructure. Co-located stacks within a single pixel are aggregated into one detection, and low-intensity or spatially compact flares may fall below the instrument's sensitivity threshold. Therefore, VIIRS-based inventories systematically underestimated flare sites, especially those that are small and close to each other [18]. High-spatial-resolution optical sensors offer a complementary pathway to address these limitations. The Multispectral Instrument (MSI) aboard Sentinel-2 satellites provides shortwave infrared (SWIR) observations at a 20 m GSD with a five-day revisit time, while the Operational Land Imager (OLI) aboard Landsat 8 and OLI–2 aboard Landsat 9 provide SWIR observations at 30 m GSD with an eight-day repeat cycle [19, 20]. At typical flare temperatures around 1,800 K, the maximum thermal emission produces a detectable radiance signal in the 2.2 µm SWIR band even under daytime solar background conditions [15]. Combined, Sentinel-2 and Landsat 8/9 yield an effective revisit time of approximately 3–5 days. Their joint application with VIIRS to annual image archives has been shown to identify substantially more flare sites than VIIRS alone, particularly for dense active sites [18, 21]. Despite this demonstrated potential, multi-sensor high-resolution approaches have not yet been systematically applied to characterize flaring activity across diverse operational contexts at the country and basin scales.

Beyond detection, the operational characteristics of flaring have important but underexplored implications for emission inventories and mitigation targeting. Key distinctions include whether a site burns continuously

or episodically, and whether it is associated with oil or gas production [22–24]. Dubey et al. [14] recently highlighted the dominant role of routine flaring in the global flaring budget and its association with flaring intensity, underscoring the value of operationally resolved flare inventories. Continuous flaring at oil production sites provides an important operational indicator of potential routine flaring, whereas episodic flaring is more commonly linked to operational events such as start-up, shutdown, maintenance, and blowdown [25]. These distinctions are important because continuous and episodic flares can differ in terms of flame stability, operating conditions, methane release potential, and mitigation options [17]. Therefore, classification frameworks that combine temporal activity patterns from VIIRS time series with fuel-type attribution from production databases offer a pathway towards operationally informative flare inventories.

The spatial relationship between flaring sites and pipeline infrastructure provides an additional interpretive dimension. Proximity to gathering pipelines and processing facilities constrains the technical and economic feasibility of gas recovery and therefore provides an important indicator of potential mitigation options [26]. Indeed, pipeline infrastructure expansion has been shown to reduce flaring intensity by more than two-thirds in the Permian Basin O&G production region [27]. Sites distant from existing networks face high incremental costs for gas monetization, whereas those in close proximity may represent lower-cost intervention opportunities. The analysis of the spatial association between flare classification and infrastructure proximity can support the prioritization of gas recovery investments; however, considerable scope remains for such an analysis to be conducted at the regional scale using satellite-derived flare inventories.

The methane dimension of flaring also remains incompletely characterized at the site level. The IEA Global Methane Tracker estimates that the O&G sector contributes approximately 120 Mt of methane per year globally [9], of which flaring-associated emissions form a significant component sensitive to combustion completeness. Recent advances in satellite methane detection, including point-source plume mapping from the United Nations Environment Programme (UNEP) IMEO Methane Alert and Response System (MARS) and Carbon Mapper, area emission products from MethaneSAT, and country-level inversion estimates from TROPOMI [28, 29], have substantially improved the observability of O&G methane at multiple spatial scales. These datasets offer an opportunity to contextualize flare activity classifications within the broader methane emission landscape, although such multi-dataset integration remains limited in the context of operationally resolved flare classification.

In this study, we combined high-spatial-resolution observations from Sentinel-2 and Landsat 8/9 with the VNF product to classify gas flaring activity across six major flaring countries, namely Iran, Saudi Arabia, Mexico, Algeria, Nigeria, and Turkmenistan. The following four operational categories were defined: continuous oil, episodic oil, continuous gas, and episodic gas flares. We further characterized the spatial association between classified flare sites and pipeline infrastructure to assess the feasibility of gas recovery across operational classes. The classifications were also contextualized against satellite-derived methane observations spanning point-source, regional, and national scales. This integrated framework advances the scientific understanding of flares as a heterogeneous emission source. It also contributes to the monitoring capabilities required to accelerate progress towards the Zero Routine Flaring by 2030 commitment.

2 Materials and Methodology

2.1 Study Area

This study examined gas flaring activities across six major hydrocarbon-producing countries: Algeria (DZA), Iran (IRN), Mexico (MEX), Nigeria (NGA), Saudi Arabia (SAU), and Turkmenistan (TKM), together with representative multisensor observations used in the framework (Figure 1). These countries account for a substantial share of global flaring volume and span diverse geological, operational, and regulatory contexts, providing a robust basis for comparative classification analysis (Figure 1a).

The countries were selected by three criteria. First, we choose countries that show consistently high flaring volumes or intensities in the World Bank Group (WBG) record. Second, there is a sufficient multisource satellite coverage, including VIIRS night-fire detections, high-resolution optical imagery, and satellite-detected methane plumes from IMEO and Carbon Mapper. Third, they represent geographically diverse major O&G producing basins. Key upstream indicators for 2024 are summarized in the Supporting Information (Figure S1). The six countries span a wide range of flaring profiles, from Iran's high flaring volume, intensity and high methane emissions to Saudi Arabia's comparatively low methane emissions despite a leading oil production, reflecting diverse operational contexts and management practices across major O&G producing basins.

Figure 1b–e illustrate the complementary observation scales used in this study for a representative flare facility area in Algeria, centered at approximately 32.936°N, 3.234°E. A high-resolution optical image make it possible to depict the spatial context on the scale of the facility (Figure 1b). The VIIRS VNP46A1 image shows the coarse spatial sampling of nighttime thermal observations (Figure 1c), whereas Landsat 8/9 OLI/OLI–2 and Sentinel-2 MSI provide finer spatial resolution SWIR radiance observations over the same zoom extent (Figure 1d,e).

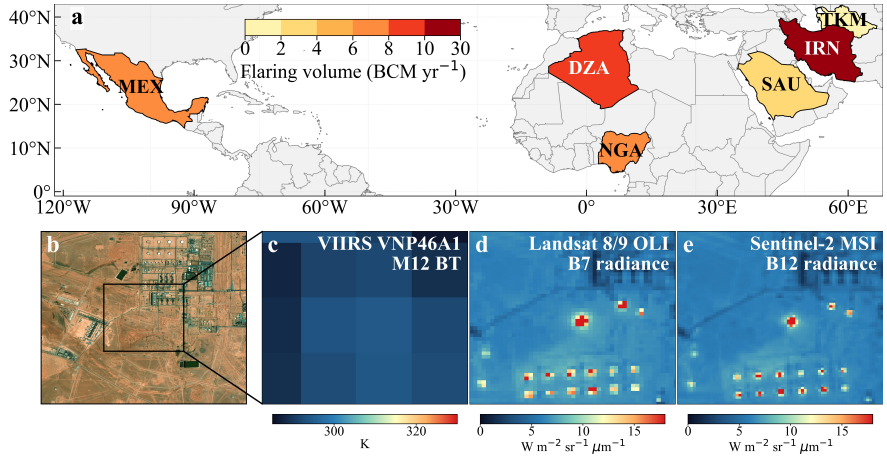


Figure 1: Selected countries and representative multisensor observations used in the framework. (a) Map of the six countries investigated, Iran (IRN), Saudi Arabia (SAU), Mexico (MEX), Algeria (DZA), Nigeria (NGA), and Turkmenistan (TKM). Country fill colors indicate annual flaring volume (BCM yr^{-1}) in 2024. (b) High resolution optical image for a representative flare facility area in Algeria, centered at approximately 32.936°N, 3.234°E. The black box marks the zoom extent shown in panels (c)–(e). (c) VIIRS VNP46A1 observation over the same area, illustrating the coarse spatial sampling of nighttime thermal observations. (d) Landsat 8/9 OLI Band 7 SWIR radiance image and (e) Sentinel-2 MSI Band 12 SWIR radiance image over the same zoom extent, showing the finer spatial detail available from high resolution imagery.

2.2 Data Sources

2.2.1 VIIRS Flaring Data

Nighttime flare detections were obtained from the VIIRS VNF product [30], distributed by the Earth Observation Group (EOG) at the Colorado School of Mines. The VNF product identifies subpixel thermal anomalies during nighttime overpasses of the Suomi-NPP, NOAA-20, and NOAA-21 VIIRS instruments operating at approximately 750 m GSD and daily revisit, by fitting a Planck blackbody function to at-sensor radiance observations across the near-infrared (NIR, M7/M8, 0.86/1.24 µm), SWIR (M10, 1.60 µm), and midwave infrared (MWIR, M12/M13, 3.74/4.07 µm) spectral bands [16, 31]. Gas flares are distinguished from other combustion sources by their characteristically high blackbody temperatures (typically >1,200 K) across repeated overpasses [15, 32]. Representative VNF daily temperature time series are shown in the Supporting Information (Figure S2). Country-level data availability and the transition from WBG flare records to classified VIIRS time-series sites are summarized in the Supporting Information (Figure S3).

In this study, the VNF information was used at three complementary levels: annual flare-volume records, multiyear site locations, and nightly per-site thermal time series. The EOG Annual Global Gas Flare Analysis provides site-level flared gas volume estimates for 2024 from the GFMR Partnership [13, 17], including field level fuel-type assignments used for four-class labelling (Section 2.3.1). The EOG Multiyear Site Catalog provides persistent geolocated site records through spatial clustering of recurring thermal anomalies [33], serving as a spatial reference for matching against high-resolution detections (Section 2.3.2). The per site nightly temporal profiles of the blackbody temperature served as the primary input for the classification of flare activities (Section 2.3.1).

Despite this complementary data structure, the utility of VIIRS-based inventories is constrained by the sensor configuration. The 750 m GSD of VIIRS introduces two limitations for detection. First, the coarse footprint may aggregate co-located flare stacks into a single pixel, causing site counts to underestimate the true number of individual sources. Second, VIIRS fails to detect small and intermittent flares below its detection limit. Seymour et al. (2025) showed that, in western Canada, industry records reported 2.2 times more flared volume and more than 14 times as many active sites as VIIRS [18]. They attributed 76% of this discrepancy to flares with flow rates below 360 m^3 h^{-1}. This finding highlights the potential under-detection of small and intermittent flares in VIIRS inventories, which is relevant to several regions examined here. These limitations motivate the complementary use of high-resolution optical imagery described below.

2.2.2 High Spatial Resolution Satellite Data

Daytime observations from Sentinel-2 MSI, Landsat 8 OLI, and Landsat 9 OLI–2 were acquired for 2024 via Google Earth Engine (GEE). Sentinel-2 MSI provides SWIR bands B11/B12 (1.61/2.19 µm) at 20 m GSD with an approximately 5-day repeat rate, while Landsat 8 OLI and Landsat 9 OLI–2 provide SWIR bands Band 6/7 (1.608/2.201 µm) at 30 m GSD with an approximately 16-day revisit per satellite. Their combined effective revisit time of approximately 3–5 days substantially improves the temporal sampling compared to either sensor on its own [21]. In the SWIR spectral region, thermal emissions from high-temperature combustion sources, such as gas flares, significantly exceed the solar-reflected background radiance, enabling subpixel flare detection in daytime imagery [19, 20]. Flare detection follows the thermal anomaly index (TAI) approach adapted from Hu et al. (2023) [34]. False positives from built-up surfaces were suppressed using the impervious surface layer extracted from the GLC_FCS30-2022 global land cover product (30 m GSD) [35]. Detailed TAI band definitions, sensor-specific spectral parameters, and the full high-spatial-resolution

flare detection workflow are provided in the Supporting Information (Section S3, Table S1, and Figure S4).

2.2.3 Methane Data

Point-source methane plume data were obtained from two publicly accessible databases. The UNEP's IMEO MARS (`https://methanedata.unep.org/`) provides expert reviewed methane plume detections from multiple satellite instruments. These include Sentinel-5P, Sentinel-2, Sentinel-3, VIIRS, EMIT, EnMAP, PRISMA, Landsat 4–9 and GOES. Carbon Mapper (`https://carbonmapper.org/`) provides daily to weekly point-source methane observations, primarily from the Tanager-1 hyperspectral imager. The database also integrates observations from EMIT and airborne platforms. Both datasets report geolocated methane plume events with emission rate estimates. Plume records are spatially matched to classified flare sites to assess co-occurrence of detectable methane emissions and active flaring (Section 2.3.3). At the regional scale, MethaneSAT Level-4 area emission products (`https://www.methanesat.org/`) are used to compare the spatial distribution of diffuse methane fluxes with flare site locations [28]. At the national scale, country-level O&G methane emission estimates from the TROPOMI inversion framework of [29] were used to contextualize flare activity within each country's total methane budget.

2.2.4 O&G Infrastructure Data

The pipeline and basin layers were obtained from the Oil and Gas Infrastructure Mapping (OGIM) database v2.7 [36], accessed via GEE. For each flare site, the distance to the nearest pipeline segment was computed to characterize infrastructure connectivity, which constrains the economic feasibility of gas recovery [12]. we note that pipelines were classified by their OGIM commodity attribute, and only gas-capable pipelines were used in the proximity analysis (Figure S5).Together with the satellite and methane products described above, these infrastructure layers constitute the multi-source dataset summarized in Table 1.

Table 1: Summary of remotely sensed and geospatial datasets used in this study.

Dataset	**Provider**	**Spatial resolution**	**Temporal resolution**
VIIRS Nightfire (VNF)	EOG	750 m (M-band)	Nightly
Sentinel-2 MSI	ESA/EU	20 m	∼5 d
Landsat 8/9 OLI/OLI–2	USGS / NASA	30 m	∼16 d
TROPOMI methane	ESA	5.5×3.5 km^2	Daily
IMEO MARS	UNEP IMEO	Point	–
Carbon Mapper	Carbon Mapper	Point	–
MethaneSAT	EDF	1 km	Tasking-based
OGIM infrastructure	EDF	Vector	–

Note: For IMEO MARS and Carbon Mapper, "Point" denotes the reported coordinate of the methane source or plume event location in the database, rather than a fixed sensor spatial resolution.

2.3 Methodology

2.3.1 Operational Classification of Flare Sites

Guided by the operational distinction between routine and non-routine flaring in the World Bank framework, and constrained by the observability of satellite datasets, the classification scheme is built on two independent,

mitigation-relevant dimensions: temporal activity pattern (continuous or episodic) and fuel type (oil or gas). Continuous flaring is more likely to indicate routine-like flaring behavior, whereas episodic flaring is commonly linked to start-up, shutdown, maintenance, or pressure-relief events. Oil-associated and gas-associated flaring differ in gas composition, infrastructure constraints, and mitigation options: continuous, high-volume oil flares provide the strongest indication of routine-like activity, episodic oil flares are more consistent with event-driven combustion, continuous gas flares most plausibly represent low-volume pilot or purge streams, and episodic gas flares are consistent with short-duration blowdown events. Based on these considerations, we defined four operational flare classes and designed a rule-based classification scheme as described below. This study focuses exclusively on upstream flaring consistent with the scope of the World Bank GFMR Partnership; downstream flaring at refineries and petrochemical plants is excluded.

For each flare site, the temporal activity pattern in 2024 was characterized using two metrics: the activity ratio and the gap score. The activity ratio $\alpha \in [0, 1]$ was used to quantify the overall temporal persistence of detectable flare activity under valid observing conditions:

$$\alpha = \frac{N_{\text{active}}}{D_{\text{valid}}}, \tag{1}$$

where N_{active} is the number of active days at the site and D_{valid} is the number of cloud-free observations in 2024. Since persistence alone does not fully capture intermittent operation, a composite gap score g was further defined to represent structural interruptions in the detection sequence. For each site, the site-level activity ratio was used as an empirical estimate of the probability of activity under otherwise unobserved cloudy conditions. Therefore, cloudy days without detections were down weighted by $(1-\alpha)$ when estimating gap duration and sparse monthly activity.

$$g = N_{\text{gaps}}^{(\delta_l)} + S_m + G_m, \tag{2}$$

where $N_{\text{gaps}}^{(\delta_l)}$ denotes the number of contiguous detection gaps longer than the long gap threshold δ_l. The terms S_m and G_m are binary indicators defined as:

$$S_m = \begin{cases} 1, & M_{\text{sparse}} > \theta_s, \\ 0, & M_{\text{sparse}} \leq \theta_s, \end{cases} \tag{3}$$

$$G_m = \begin{cases} 1, & \Delta_{\max} > \delta_m, \\ 0, & \Delta_{\max} \leq \delta_m. \end{cases} \tag{4}$$

Here, M_{sparse} is the number of calendar months with sparse detections, θ_s is the sparse month threshold, $\Delta_{\max}$ is the duration of the longest single detection gap, and δ_m is the secondary gap duration threshold. The two binary indicators account for irregular monthly coverage and extended single gap events, respectively.

The activity ratio and gap score were discretized into ordinal tiers and jointly mapped to a binary temporal label, Continuous or Episodic, using a 3×3 rule table (Table S2). The empirical distributions of the temporal metrics and placement of the selected thresholds are provided in the Supporting Information (Figure S6, Table S3), together with the rule table (Figure S7). Since the Episodic label is partly determined by temporal gaps in the daily VNF record, the interpretation of these gaps is an important source of classification uncertainty. The residual influence of cloudy days on Episodic classifications was assessed using bounding sensitivity scenarios in the Supporting Information (Section S6, Figure S8, Figure S9, Table S4). Before

integration with high-spatial-resolution detections, the spatial distribution and country level composition of the classified VIIRS sites are summarized in the Supporting Information (Figure S10).

The fuel type is assigned by spatially matching each flare site to the nearest record in the WBG flare volume dataset within a matching radius; sites without a match within this radius were labeled as unclassified. The four resulting operational classes have distinct operational interpretations and are not directly equivalent to the World Bank's flaring definitions [25]. However, they serve as satellite-observable proxies for operational behavior, as discussed in Section 3.3.

To assess the robustness of the rule-based classification, we compared its class labels with labels produced by k-means clustering, hierarchical clustering, label propagation, and self-training. Robustness was evaluated using percentage agreement, Cohen's kappa, adjusted Rand index, and normalized mutual information. Results are reported in the Supporting Information (Table S5).

2.3.2 Cross-Sensor Matching of VIIRS and High-Resolution Flare Detections

The VIIRS flare site locations from the EOG Multiyear Site Catalog served as the spatial reference for integrating high-resolution Sentinel-2 and Landsat 8/9 detections. For each VIIRS site, high-resolution detections within a 1 km radius were aggregated. The matching distance sensitivity analysis in the Supporting Information (Figure S11) supports the use of the 1 km matching radius. This radius was used as a spatial matching tolerance, not as a criterion for separating individual flare stacks within a VIIRS pixel. The integration exploits the complementary strengths of each sensor. VIIRS provides nightly thermal detection and temporal activity records required for activity classification. Sentinel-2 and Landsat 8/9 provide daytime confirmation of persistent combustion sources at 20–30 m resolution. These high-resolution detections allow flare activity to be localized more precisely and enable additional fine-scale detections to be mapped. This matching step produced a unified flare inventory by combining high-resolution spatial localization with VIIRS temporal activity records. High-resolution detections without corresponding VIIRS sites were retained as supplementary detections but were not used for VIIRS-based temporal classification. Figure 2 shows that 50–70% of VIIRS sites are matched to more than one Sentinel–2 or Landsat 8/9 detection within 1 km. This indicates that a substantial fraction of VIIRS sites represents fine-scale flare clusters rather than one-to-one matches. These results demonstrate the added value of Sentinel-2 and Landsat 8/9 for improving spatial detail in the flare inventory. The detailed country-level count comparison between VIIRS and high-resolution detections is documented in the Supporting Information (Figure S12).

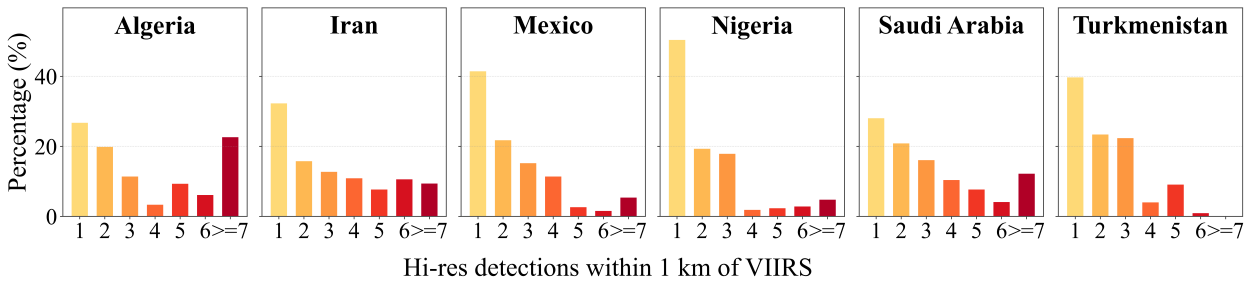


Figure 2: The distribution of high-spatial-resolution flare detections matched to individual VIIRS flare sites across each investigated country in 2024. For each country, the x-axis indicates the number of Sentinel-2 and Landsat 8/9 detections located within 1 km of a VIIRS site, grouped from one detection to seven or more detections. The y-axis shows the percentage of VIIRS sites in each bin.

2.3.3 Infrastructure Proximity and Methane plume Co-location

(1) Pipeline Proximity.

The Euclidean distance to the nearest gas pipeline segment in the OGIM database is computed for each classified flare site. Sites were grouped using distance thresholds of 1, 2, 5, 10, and 15 km to describe infrastructure proximity across operational classes. Pipeline proximity is used as an indicator of potential gas recovery feasibility, because shorter distances generally imply lower additional infrastructure requirements. The resulting distance distributions were then compared across continuous and episodic flare classes to evaluate whether operational patterns differed in their proximity to existing gas-transport infrastructure.

(2) Methane Plume Co-location.

Since flare sites can be spatially clustered within dense production facilities, methane plumes from the IMEO and Carbon Mapper databases were matched to classified flare sites using a conservative 100 m radius to limit ambiguous assignments between nearby sources. Because coarse-resolution sensors cannot resolve individual flare sites, we retained only plumes detected by instruments with a spatial resolution of 60 m or finer and excluded detections from Sentinel-5P, Sentinel-3, VIIRS, and GOES. Matched flare site and methane plumes count are calculated for each operational class at the country level. Matched flare volumes from the GFMR dataset were aggregated to quantify the volumetric significance of co-located flaring activity. This co-location analysis provides an independent observational basis for comparing flare classes with satellite-detected methane emissions. It was used to evaluate the spatial consistency between classified flare sites and methane plume detections across operational classes and countries.

3 Results and Discussion

3.1 Spatial Distribution and Classification of Flare Sites

The rule-based labels show high agreement with two semi-supervised methods (label propagation and self-training) and lower agreement with two unsupervised clustering methods (k-means and hierarchical clustering; Table S5). After matching the VIIRS classification result and High-spatial-resolution satellite detections, we identified 1,910 flaring sites across the six investigated countries, approximately 1.8 times the number detected by VIIRS alone (Figure 3, Figure S12).

We first examine site counts and VIIRS flare volumes at the country and basin level (Figure 3). Iran has the largest number of detected sites (655; Figure 3b). The Zagros Foldbelt (ZAF) basin alone accounts for 519 of these sites. It contributes 18,738 Mm^3 of flare volume, the dominant share of the national total. Algeria follows with 436 sites across five basins (Figure 3a). The Illizi–Ghadames (ILG) and Oued Mya (OUM) basins lead, with 222 and 105 sites. They contribute 3,804 and 2,502 Mm^3 of flare volume, respectively. Saudi Arabia has 334 sites (Figure 3e). Most are concentrated in the Widyan–North Arabian Gulf (WNA) basin, with 296 sites and 1,983 Mm^3 of flare volume. Nigeria has 205 sites (Figure 3d) that are entirely concentrated in the Niger Delta (NID) basin. Mexico has 183 sites (Figure 3c), with the largest share in Macuspana (MAC) basin (110 sites). Turkmenistan has 97 sites (Figure 3f). Most are concentrated in the Amu-Darya (AMU) and South Caspian (SOC) basins. These basins contribute 375 and 951 Mm^3 from 69 and 24 sites, respectively. The basin abbreviations used in the analyses are listed in the Supporting Information (Table S6). Within these leading basins, flare class composition differs by category, both in flare site count and in flare volume. As shown in the pie charts in Figure 3, continuous oil flares dominate several basins across different countries. This includes ILG and OUM basins in Algeria, ZAF in Iran, MAC

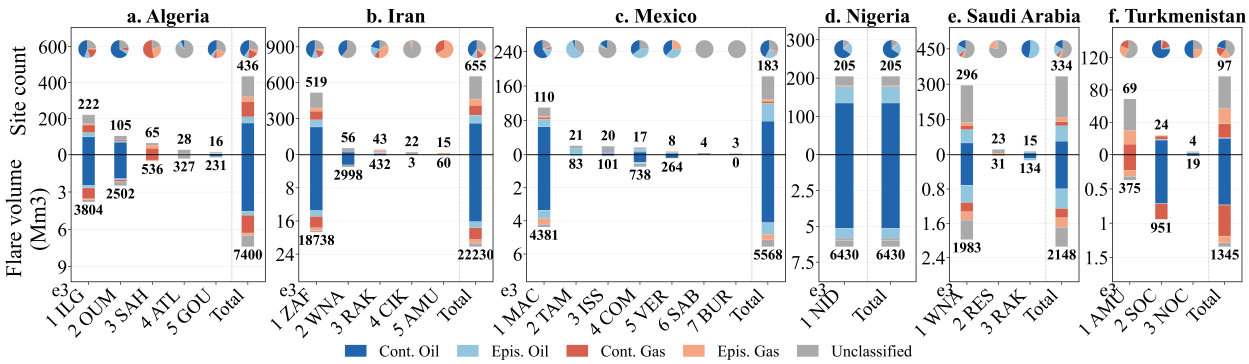


Figure 3: Basin-level summaries of classified high-spatial-resolution flare-site counts and VIIRS-based flare volumes within the labelled sedimentary basins in each country. For each basin and nation, the pie charts show the class composition. Upper stacked bars show site counts, and lower stacked bars show VIIRS-based flare volumes (Mm^3), both disaggregated by its operational class. Full basin names and abbreviations are provided in the Supporting Information (Table S6).

in Mexico, and SOC in Turkmenistan. Episodic oil flare count are more prominent in other few basins, including Tampico–Misantla–Magiscat (TAM) basin and Comalcalco (COM) basin in Mexico and Rub Al Khali (RAK) basin in Saudi Arabia. Gas flares, both continuous and episodic, are a minority class in most basins. Sahara (SAH) basin in Algeria and AMU basin are exceptions, where continuous gas flare dominates and episodic gas flare dominates, respectively. But SOC, a nearby basin in Turkmenistan, shows a different pattern. SOC holds only 24 sites, but it contributes the country's largest single-basin volume (951 Mm^3). This volume is dominated by continuous oil flares. Site count and flare volume can therefore be decoupled within the same country.

These class differences also have a distinct spatial pattern within each basin (Figure 4). Continuous oil sites tend to form dense, spatially compact clusters. This is visible along the core of the ZAF basin in Iran (Figure 4b). Gas flare sites are more spatially dispersed. This pattern is clearest in the AMU basin in Turkmenistan (Figure 4f), where continuous and episodic gas flares are spread across the basin. In more heterogeneous basins such as WNA basin in Saudi Arabia (Figure 4e), different classes are spatially intermixed rather than forming separate sub-clusters. This suggests fine-scale operational variability within a single basin. The ridge plots above the country maps in panels (a)–(f) show the distribution of flare volumes for each operational class. Episodic flares show the opposite pattern to continuous flares at the volume level. Their site counts are non-negligible. But they make up a smaller fraction of total flare volume in all six countries. The ridge plots for episodic classes in Figure 4 are left-shifted relative to their continuous counterparts. Median per-site volumes for episodic flares are below 10 Mm^3. This is consistent with intermittent operational origins such as well testing, upset conditions, or emergency pressure relief [37, 38]. The volumetric gap between continuous and episodic classes spans one to two orders of magnitude across all countries. This confirms that mitigation efforts targeting the continuous flare population would yield the greatest emission reductions per site addressed.

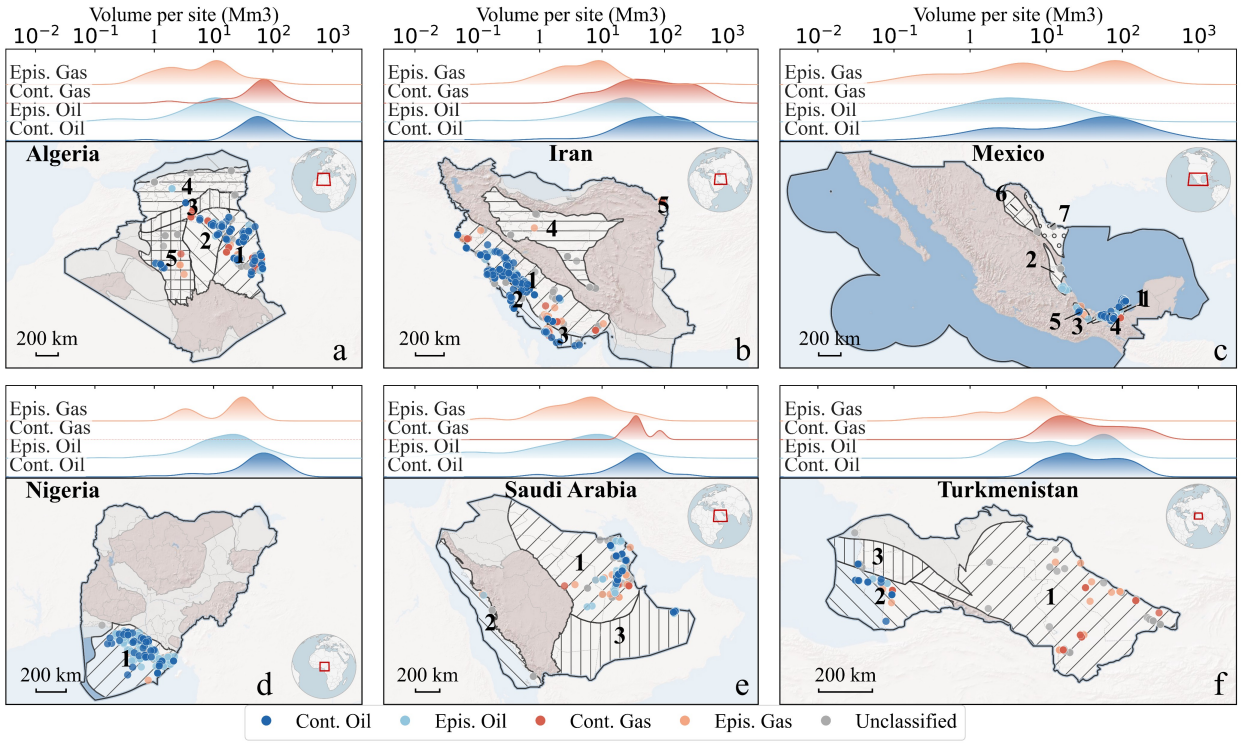


Figure 4: Spatial distribution, class-specific volume distributions, and basin-level composition of flare sites across the six investigated countries. In each country panel, points indicate high-spatial-resolution flare detections colored by their operational class: continuous oil, episodic oil, continuous gas, episodic gas, and unclassified. Numbered polygons indicate sedimentary basins; full basin names and abbreviations are provided in the Supporting Information (Table S6). Ridge plots above panels (a)–(f) show the kernel density distributions of per-site VIIRS flare volume (Mm^3) by operational class on a logarithmic x-axis.

3.2 Analysis between Flaring Activity Types, Facility and Methane Emissions

3.2.1 Pipeline Proximity of Classified Flare Sites

Figure 5 presents the cumulative distribution of flare site counts (panel a) and flare volumes (panel b) across five pipeline distance thresholds ($\leq$1, 2, 5, 10, and 15 km) by operational class. This gradient approach avoids imposing an arbitrary recovery feasibility cutoff and characterizes the full proximity landscape to prioritize measures at the country level.

The volume patterns differ substantially among countries. Iran shows the strongest cumulative flare volume. In Iran, volumes accumulate steeply at close range, from 1,361 Mm^3 at $\leq$1 km to 6,299 Mm^3 at $\leq$5 km, driven mainly by continuous oil flares. This proximity to existing pipeline infrastructure indicates that a moderate expansion of the network could enable the recovery of a substantial flare volume. This pattern suggests that existing pipeline proximity may provide an important screening criterion for recovery potential. Algeria also contributes a substantial flare volume near gas pipeline. The volumes increased more gradually from 1,617 to 4,808 Mm^3 across all distance steps.

Saudi Arabia shows a different structural pattern. While episodic oil flares dominate in terms of site counts across all distance steps, their per-site volumetric contribution is disproportionately low. The near-

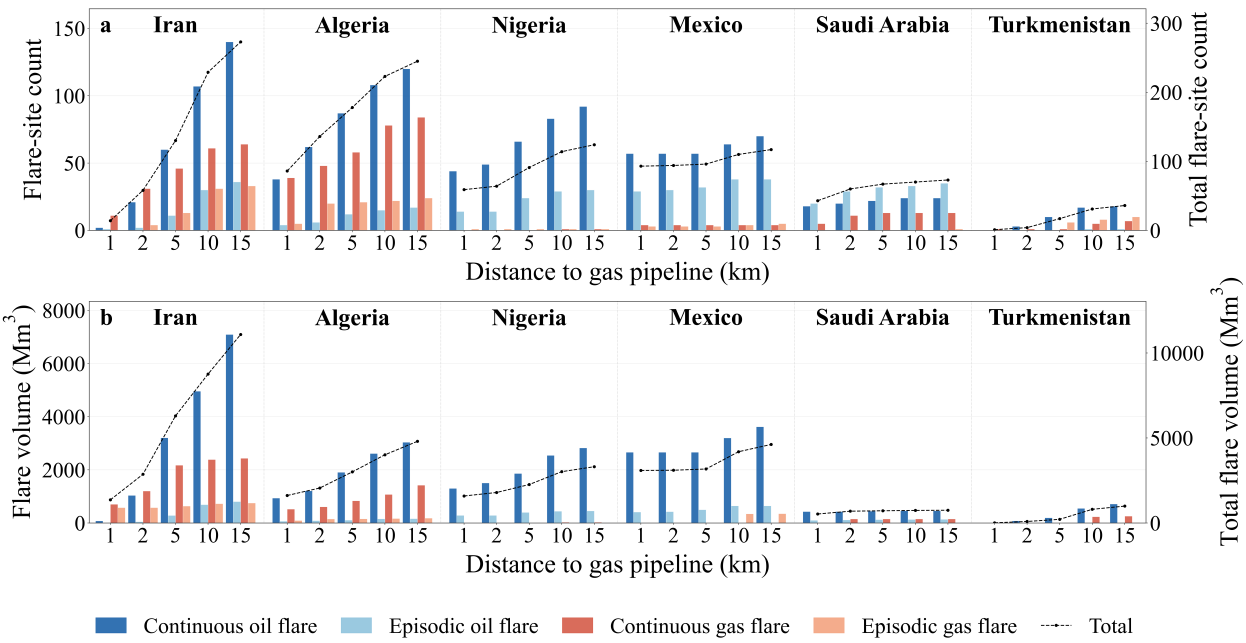


Figure 5: Proximity of upstream flare sites to gas pipelines across the six investigated countries. Flare sites within sedimentary basins were binned by the distance to the nearest gas pipeline at 1, 2, 5, 10, and 15 km thresholds. (a) Site count by operational class and cumulative total number from high-resolution Sentinel-2 and Landsat 8/9 detections. (b) Flaring volume ((Mm^3) by operational class and cumulative total from VIIRS-based classifications matched to WBG estimates. Countries are ordered by decreasing total site count at 15 km.

uniform distribution across 1–15 km indicates that pipeline proximity does not effectively discriminate flaring intensity. This is consistent with the operational origins of episodic flare events driven by maintenance, start-up, and equipment overpressure events, rather than continuous gas production. Infrastructure-based recovery, therefore, offers limited leverage in these contexts, regardless of distance.

Mexico presents a distinctive front-loaded pattern: 3,102 Mm^3, approximately 68% of the total volume at $\leq$15 km is already reached by $\leq$2 km and is concentrated in continuous oil flares. The feasibility of connecting flare sites to pipeline infrastructure depends strongly on both, extension distance and available gas volume per site. Therefore, the spatial concentration of flare volume within $\leq$2 km indicates that Mexico has a comparatively favorable near-term recovery opportunity among the six countries investigated.

Turkmenistan has the lowest absolute counts (36 sites) and volumes (994 Mm^3) at $\leq$15 km, with a notable fraction of gas flares beyond 5 km, reflecting the dispersed infrastructure of the AMU basin. Where per-site flare volumes are small and pipeline networks are sparse, a pipeline connection is less likely to be economically feasible. In these settings, an improvement of on-site combustion or a small-scale fuel conversion may provide more practical options for reducing methane emissions.

These results underscore the need for a country-specific analysis, as the relationship of proximity-mitigation varies substantially across production contexts. Iran and Algeria present the strongest cases for infrastructure extension, given Iran's steep near-pipeline volumetric accumulation and Algeria's higher flare site count and higher flare volume within 2 km. In this case, a modest expansion of gathering capacity could unlock substantial gas recovery and avoid large quantities of associated GHG emissions. Mexico offers a narrow but highly cost-effective recovery window within $\leq$2 km. Saudi Arabia is constrained by

the dominance of low-volume episodic flares at all distances. Turkmenistan faces additional barriers due to infrastructure sparsity and low per-site volumes, where on-site combustion improvement may be more practical than pipeline connections. In Iran, Algeria, and Turkmenistan, continuous flares consistently had higher per-site volumes than episodic flares, representing the primary targets for infrastructure-based emission reduction. This raises the question of whether persistent flaring activity translates into detectable atmospheric methane enhancements, which is examined in the following section.

3.2.2 Spatial Co-location of Flare Sites with Methane Plumes Detected by Satellites

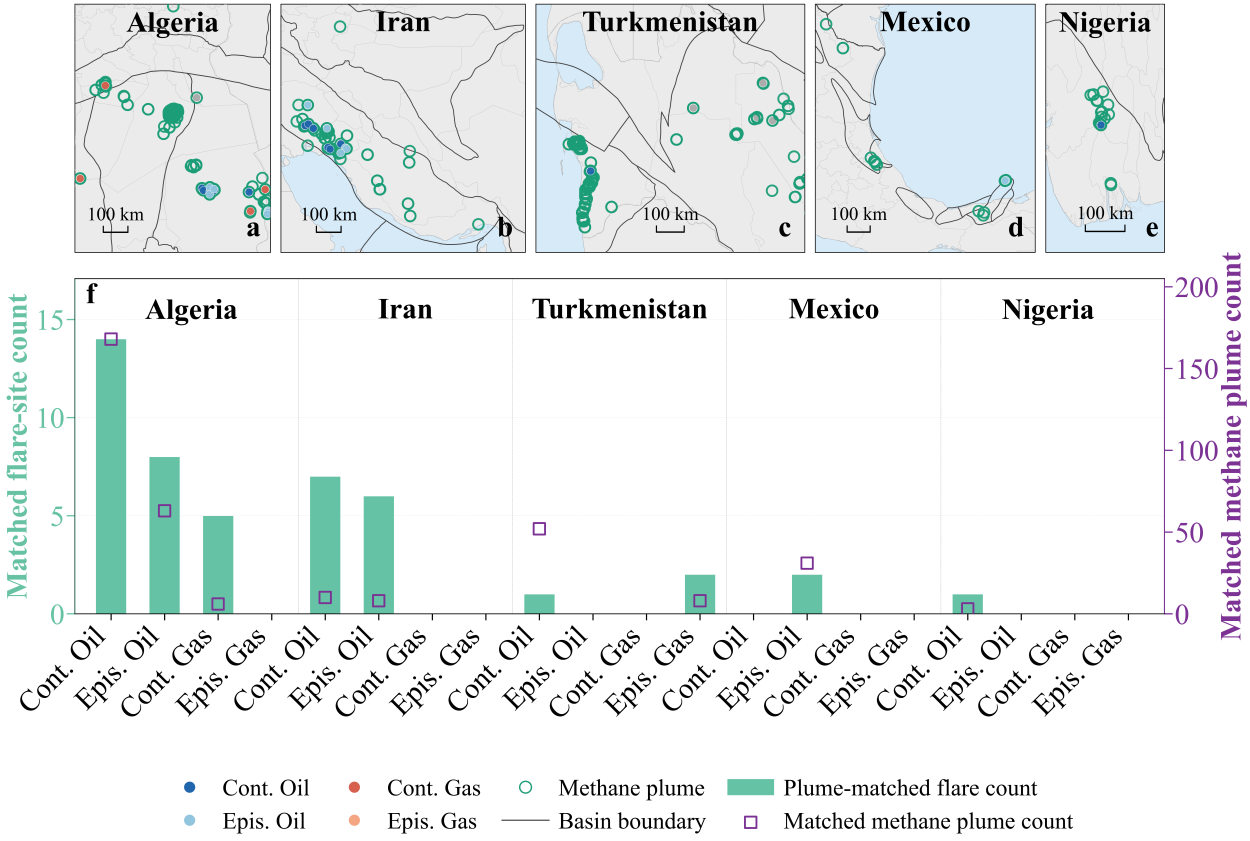


Figure 6: Spatial co-location between classified flare sites and methane plumes in 2024. Five of the six investigated countries are shown. Saudi Arabia is omitted because no flare site was matched to a methane plume. (a)–(e) Country-level zoom panels for Algeria, Iran, Turkmenistan, Mexico, and Nigeria. Filled points represent flare sites by operational class; hollow circles indicate methane plumes from IMEO and Carbon Mapper, while dark lines show boundaries of sedimentary basins. (f) Summary of plume-matched flare counts and matched count of methane plumes by country and the operational flare class. Bars show the number of classified flare sites matched to methane plume detections.

Methane emissions from flaring operations represent a significant and often under-characterized component of upstream sector emissions of hydrocarbons. However, the relationship between the flare operational behavior and methane detectability remains poorly constrained at the site level. To address this, we spatially matched classified flare sites against methane plumes detected from IMEO and Carbon Mapper, recording a match when the nearest detected plume location fell within 100 m of a classified flare site. As a complementary area-source perspective, the Supporting Information (Figure S13) shows the spatial relationship

between classified flare sites and the MethaneSAT gridded methane flux retrievals. This provides an operational source context for interpreting regional methane hotspots and assessing where persistent flaring activity may contribute to O&G methane emissions [28]. The analysis revealed systematic differences in methane plume co-location across flare operational classes and country contexts. These spatial patterns provide evidence for emission-source interpretation and mitigation prioritization (panels (a)–(e) in Figure 6).

Among the matched pairs, continuous flare classes accounted for the majority of matched site counts and flare volumes, indicating that persistent flaring activity is more frequently co-located with satellite-detected methane enhancements than episodic activity (Figure 6f).

In Algeria, for instance, continuous oil flares alone yield 14 plume-matched sites, with corresponding matched volumes of 532.46 Mm^3. Episodic oil and continuous gas classes contributed an additional 140.70 Mm^3 and 175.94 Mm^3 respectively (Supporting Information, Figure S14). This multi-class co-location pattern was concentrated in the ILG and OUM basins (Figure 4a), reflecting the operational diversity of Algeria's flaring activity. The spatial concentration of matched detections across multiple flare classes within a confined basin area is consistent with the documented role of super-emitting upstream facilities in the methane budget [39].

Iran exhibits a more concentrated co-location structure. 7 plume-matched continuous oil flares in the southwestern Zagros region accounted for matched volumes of 1,062.40 Mm^3, accompanied by average flux rates approaching 6,754.37 kg hr^{-1}. This combination of large matched flare volumes and high methane flux rates suggests that a limited number of high-intensity oil-producing areas are disproportionately co-located with methane plumes. MethaneSAT area-source methane context further shows this pattern in the Supporting Information (Figure S13).

Turkmenistan presents a structurally distinct pattern. At the country level, most classified sites are gas flares in the AMU basin, whereas the largest matched flare volume comes from fewer continuous oil sites in the SOC basin. Most methane plumes over Turkmenistan are not co-located with any active flare site (Figure 6c). These plumes may originate from other sources, such as inactive flares and gas disposal facilities venting gas, or pipeline leaks, as defined in the source level information in IMEO's emission source database. This is consistent with the findings reported by Irakulis-Loitxate et al. (2022) [40], which observed a decrease in active flaring over time correlated with an increase in methane emissions from those same sources in the SOC basin. This demonstrates that the observed reduction in flaring does not necessarily indicate a change in operations toward better use of the gas, and may be indicative of a larger problem where gas is being vented rather than flared. This showcases the importance of analyzing flaring patterns with methane emission observations. Among matched plumes, episodic gas flares account for slightly more matched sites than continuous oil flares, but most matched methane plumes are associated with a single continuous oil site in the SOC basin. However, matched flare volume and average CH_4 flux rate do not necessarily identify the same priority sites (Figure S14), so mitigation interpretation here should weigh both, rather than volume alone.

In Mexico and Nigeria, the co-location is restricted entirely to oil flare classes. Mexico recorded 2 matched episodic oil flares and 31 matched methane plumes, with matched flare volumes of 44.44 Mm^3. Nigeria only has 1 plume-matched continuous oil flare site, contributing a flare volume of 15.59 Mm^3. In both countries, the matched plumes were spatially clustered within narrow geographic zones (Gulf of Mexico coastal corridor and NID basin). This pattern suggests that methane emissions from flaring activities are highly localized and amenable to spatially targeted monitoring and follow-up inspections. Saudi Arabia has no co-location signal across all classes. This is consistent with Saudi Arabia's predominantly episodic, lower-volume flaring

characteristics and correspondingly limited detectability of methane plumes.

Two cross-cutting implications emerge from this analysis. First, the methane-plume co-location is mainly more consistently associated with oil flare classes than with gas flare classes. This pattern indicates that oil flaring is a useful operational indicator for identifying locations where methane enhancements are more likely to be observed. Second, countries where co-location spans multiple flare classes and large matched flare volumes, particularly Algeria and Iran, provide evidence for integrating operational flare classification with methane plume observations. We note that plume detection frequency depends on both the occurrence of emissions and the number of satellite observations. Since most plume-detecting missions operate through targeted tasking, observation density is not uniform across countries, and absolute plume counts should be compared with this in mind.

3.3 Implications and Future Directions

Operational Flare Classification as a Mitigation Targeting Tool. The four-class typology introduced in this study provides operationally differentiated intelligence for mitigation prioritization. Within the Zero Routine Flaring by 2030 framework, routine flaring is specifically defined as the continuous combustion of gas and oil production sites in the absence of sufficient infrastructure to reinject, utilize, or dispatch produced gas to market [25]. Under this definition, the continuous oil flares identified in this study are the class that most likely represents routine flaring. That disproportionately contribute to the total flare volume across all six countries underscoring their primacy as mitigation targets. In contrast, episodic oil flares more plausibly correspond to non-routine or safety flaring associated with operational events such as start-up, maintenance, and pressure relief, for which the appropriate intervention is process optimization rather than infrastructure investment [37]. Continuous gas flares, which are comparatively rare, most likely represent pilot or purge volumes rather than large-scale routine gas disposals, whereas episodic gas flares are consistent with short-duration blowdown events at gas production and processing facilities. However, it should be noted that a purely satellite-based classification cannot fully distinguish routine from safety flaring within continuous classes: large-volume continuous flares at oil production sites provide the strongest inferential basis for routine flaring, whereas lower-volume continuous sources may include persistent safety or purge streams. This limitation reinforces the need to interpret the classification in conjunction with facility-level production contexts and infrastructure data.

Continuous flares accounted for a disproportionate share of the total flare volume relative to the site count across all six countries. Mitigation frameworks that prioritize continuous oil flare suppression or gas recovery would achieve the greatest volumetric reductions per site addressed [26, 27]. The distinction between oil and gas flaring further informs technology selection. Continuous oil flares are the primary candidates for pipeline tie-ins and gas recovery. Gas flares in gas-dominated basins, such as the AMU basin, may be more amenable to on-site combustion improvement or small-scale fuel conversion.

Basin-Level Flare Concentration and the Case for Targeted Interventions. The basin-level butterfly charts in Figure 3 indicate that flare volumes are highly concentrated in a small number of production basins. In Iran, the ZAF basin accounts for 18,738 Mm^3 of flare volume, while Nigeria, Saudi Arabia, Mexico, and Turkmenistan are similarly dominated by one or two high-volume basins. This spatial concentration suggests that mitigation strategies focused on the highest-volume basin clusters may achieve larger reductions than spatially diffuse, national-scale interventions.

The pipeline proximity analysis further refines this interpretation by identifying the locations of concentrated flare volumes near the existing gas-transport infrastructure. In Iran and Algeria, a substantial

share of flare volumes occurs within moderate extension distances from existing pipelines, suggesting that infrastructure-based gas recovery may be more feasible in these areas than in more remote flare clusters. In Mexico, the rapid accumulation of flare volumes within short pipeline distances indicates a particularly favorable near-term opportunity for recovery and utilization. These results support the broader principle that gas-gathering and processing infrastructure should be planned alongside production expansion to reduce the risk of stranded flare volumes in O&G producing basins. This targeted mitigation perspective is consistent with recent global estimates [14]. Flare recovery at a relatively small number of high-volume sites can deliver substantial economic value alongside significant emission reductions.

Integration of Flare Classification with Satellite Methane Monitoring. A Spatial co-location analysis demonstrated that operational flare classification provides useful source-context information for interpreting methane plumes detected by satellite. High methane plume match rates were observed across multiple flare classes in Algeria and Turkmenistan. This positions the flare classification framework as a useful contextual layer for satellite-based emission attribution. Regulators and operators can thereby prioritize inspections and interventions at sites most likely associated with large methane plumes. The divergence between the match patterns in Iran and Turkmenistan underscores the value of class-resolved rather than aggregate flare inventories for methane accounting purposes. As the density and revisit frequency of point-source methane detection satellites continue to increase, integrating operationally classified flare inventories with near-real-time plume data offers a pathway toward continuous, verifiable monitoring of O&G methane emissions at the facility level.

Limitations and Future Directions. Despite all the positive results, there are some limitations in the current analysis. The VIIRS based flare volume estimates carry an inherent uncertainty from the empirical radiance-to-volume conversion, and small or low-temperature flares below the VIIRS detection threshold may be systematically under-represented in dense production areas. Also, satellite-based classifications cannot principally distinguish routine from safety flaring within continuous classes. High-volume continuous oil flares provide the strongest basis for inferring routine gas disposal, but lower-volume continuous sources may represent persistent safety or purge streams that are not amenable to the same mitigation logic. Furthermore, temporal classification may be sensitive to non-detections under optically thick cloud conditions. This limitation is most relevant for episodic sites, where cloud-related gaps may resemble true intermittent operation. We therefore quantified cloudy not detectable fractions for episodic sites as a separate uncertainty diagnostic in the Supporting Information (Section S6). Its effect on the classification was limited in most countries and most pronounced in Nigeria, where cloud cover is frequent (Figure S8, Table S4). Additionally, the temporal scope of the analysis reflects a fixed observational window; flare classification may shift over time as production profiles evolve, infrastructure is added, or regulatory conditions change. Finally, pipeline proximity serves only as a preliminary indicator of gas recovery feasibility. Although we restricted the analysis to gas-capable pipelines, pipeline composition varies widely across countries (Figure S15). Actual recovery also depends on pipeline capacity, operating pressure, gas composition, and access to compressor stations and processing facilities. These data are rarely available publicly. Future analyses could integrate them to refine recovery estimates.

Future studies should address these limitations in several ways. Extending the classification to additional major flaring countries and tracking class-resolved inventories over multi-year periods would enable the quantification of progress toward zero routine flaring. It would also identify the production contexts in which routine flaring persists or intensifies. Developing volume calibration methods for high-resolution Sentinel-2 and Landsat 8/9 detections, analogous to existing VIIRS-based approaches, would allow per-site volume

attribution at spatial scales inaccessible to current coarse-resolution products. Finally, the integration of operational classes with methane observations, from point-source plumes to area fluxes, could be extended to additional basins and multi-year records. This would strengthen the link between flare behavior and regional methane budgets. It would also support verifiable reporting of climate commitments at national and global scales.

Acknowledgements

This research was supported by the China Scholarship Council (grant number:202306220072), the UNEP's International Methane Emissions Observatory (IMEO) (grant number: DTIE23-EN6386) and the Spanish Ministry of Science, Innovation and Universities (grant PID2023-148485OB-C21/C22 funded by MCIU/AEI/10.13039/501100011033 ERDF, EU).

Supporting Information

The Supporting Information is available free of charge, including:

(S1) The indicator from upstream sector;
(S2) Exploration of VIIRS data;
(S3) Flare site detection with Sentinel-2 and Landsat;
(S4) OGIM Pipeline for gas recovery;
(S5) Classification of VIIRS sites;
(S6) Cloud-related sensitivity in episodic classifications;
(S7) Summary of VIIRS classification results;
(S8) Robustness evaluation;
(S9) Flare count matching and comparison;
(S10) Abbreviation of basin names;
(S11) Area-source methane detection with MethaneSAT;
(S12) Matched flare volume and flux rate of methane plume;
(S13) Pipeline commodity composition by country.

References

(1) Fawole, O. G.; Cai, X. .-.; MacKenzie, A. R. Gas flaring and resultant air pollution: A review focusing on black carbon. *Environmental Pollution* **2016**, *216*, 182–197.

(2) Gvakharia, A.; Kort, E. A.; Brandt, A.; Peischl, J.; Ryerson, T. B.; Schwarz, J. P.; Smith, M. L.; Sweeney, C. Methane, Black Carbon, and Ethane Emissions from Natural Gas Flares in the Bakken Shale, North Dakota. *Environmental Science & Technology* **2017**, *51*, 5317–5325.

(3) Caseiro, A.; Gehrke, B.; Rücker, G.; Leimbach, D.; Kaiser, J. W. Gas flaring activity and black carbon emissions in 2017 derived from the Sentinel-3A Sea and Land Surface Temperature Radiometer. *Earth System Science Data* **2020**, *12*, Publisher: Copernicus GmbH, 2137–2155.

(4) Hecobian, A.; Clements, A. L.; Shonkwiler, K. B.; Zhou, Y.; MacDonald, L. P.; Hilliard, N.; Wells, B. L.; Bibeau, B.; Ham, J. M.; Pierce, J. R.; Collett, J. L. J. Air Toxics and Other Volatile Organic Compound Emissions from Unconventional Oil and Gas Development. *Environmental Science & Technology Letters* **2019**, *6*, 720–726.

(5) Irakulis-Loitxate, I.; Gorroño, J.; Zavala-Araiza, D.; Guanter, L. Satellites Detect a Methane Ultra-emission Event from an Offshore Platform in the Gulf of Mexico. *Environmental Science & Technology Letters* **2022**, *9*, Publisher: American Chemical Society, 520–525.

(6) Plant, G.; Kort, E. A.; Brandt, A. R.; Chen, Y.; Fordice, G.; Gorchov Negron, A. M.; Schwietzke, S.; Smith, M.; Zavala-Araiza, D. Inefficient and unlit natural gas flares both emit large quantities of methane. *Science* **2022**, *377*, 1566–1571.

(7) Plant, G.; Kort, E. A.; Gorchov Negron, A. M.; Chen, Y.; Fordice, G.; Harkins, C. In Situ Sampling of NOx Emissions from United States Natural Gas Flares Reveals Heavy-Tail Emission Characteristic. *Environmental Science & Technology* **2024**, *58*, 1509–1517.

(8) In *Global Warming of 1.5°C: IPCC Special Report on Impacts of Global Warming of 1.5°C above Pre-industrial Levels in Context of Strengthening Response to Climate Change, Sustainable Development, and Efforts to Eradicate Poverty*, Intergovernmental Panel on Climate Change (IPCC), Ed.; Cambridge University Press: Cambridge, 2022, pp 541–562.

(9) Global Methane Tracker 2025 – Analysis, IEA `https://www.iea.org/reports/global-methane-tracker-2025` (accessed 06/16/2026).

(10) Fann, N.; Baker, K. R.; Chan, E. A. W.; Eyth, A.; Macpherson, A.; Miller, E.; Snyder, J. Assessing Human Health PM2.5 and Ozone Impacts from U.S. Oil and Natural Gas Sector Emissions in 2025. *Environmental Science & Technology* **2018**, *52*, 8095–8103.

(11) Aliyu, A.; Alhems, L. M.; Mohammed, A. Assessment of Effective Dose in the Oil and Gas Industry of Saudi Arabia. *ACS Chemical Health & Safety* **2025**, *32*, 522–529.

(12) About the ZRF, World Bank `https://www.worldbank.org/en/programs/zero-routine-flaring-by-2030/about` (accessed 06/16/2026).

(13) About GFMR, World Bank `https://www.worldbank.org/en/programs/gasflaringreduction/about` (accessed 06/16/2026).

(14) Dubey, L.; Davis, M.; Balcombe, P. How much are we really flaring? A new gas flare tracker and the first estimates of 2025 global flaring. *ChemRxiv* **2026**, *2026*, DOI: `10.26434/chemrxiv.15005027/v1`.

(15) Elvidge, C.; Zhizhin, M.; Baugh, K.; Hsu, F.-C.; Ghosh, T. Methods for Global Survey of Natural Gas Flaring from Visible Infrared Imaging Radiometer Suite Data. *Energies* **2015**, *9*, 14.

(16) Elvidge, C.; Zhizhin, M.; Hsu, F.-C.; Baugh, K. VIIRS Nightfire: Satellite Pyrometry at Night. *Remote Sensing* **2013**, *5*, 4423–4449.

(17) Zhizhin, M.; Elvidge, C. D.; Sparks, T.; Ghosh, T.; Bazilian, M.; Hsu, F.-C. An Improved Calibration for Satellite Estimation of Flared Gas Volumes from VIIRS Nighttime Data. *Energies* **2025**, *18*, Publisher: Multidisciplinary Digital Publishing Institute.

(18) Seymour, S. P.; Aylward, B.; Galvin, K. P.; Kang, M.; Xie, D. Gas Flaring Is Likely Underestimated by Satellites due to Undetected Small Flares. *Environmental Science & Technology* **2025**, *59*, Publisher: American Chemical Society, 21465–21475.

(19) Faruolo, M.; Falconieri, A.; Genzano, N.; Lacava, T.; Marchese, F.; Pergola, N. A Daytime Multisensor Satellite System for Global Gas Flaring Monitoring. *IEEE Transactions on Geoscience and Remote Sensing* **2022**, *60*, Conference Name: IEEE Transactions on Geoscience and Remote Sensing, 1–17.

(20) Liu, Y.; Zhi, W.; Xu, B.; Xu, W.; Wu, W. Detecting high-temperature anomalies from Sentinel-2 MSI images. *ISPRS Journal of Photogrammetry and Remote Sensing* **2021**, *177*, 174–193.

(21) Faruolo, M.; Genzano, N.; Marchese, F.; Pergola, N. Multi-Temporal Satellite Investigation of gas Flaring in Iraq and Iran: The DAFI Porting on Collection 2 Landsat 8/9 and Sentinel 2A/B. *Sensors* **2023**, *23*, Publisher: Multidisciplinary Digital Publishing Institute, 5734.

(22) Lavoie, M.; Perine, G.; Risk, D. Methane emissions from inactive oil and gas wells in Western Canada. *Environmental Monitoring and Assessment* **2026**, *198*, 412.

(23) Ialongo, I.; Stepanova, N.; Hakkarainen, J.; Virta, H.; Gritsenko, D. Satellite-based estimates of nitrogen oxide and methane emissions from gas flaring and oil production activities in Sakha Republic, Russia. *Atmospheric Environment: X* **2021**, *11*, 100114.

(24) Liu, R. E.; Ravikumar, A. P.; Bi, X. T.; Zhang, S.; Nie, Y.; Brandt, A.; Bergerson, J. A. Greenhouse Gas Emissions of Western Canadian Natural Gas: Proposed Emissions Tracking for Life Cycle Modeling. *Environmental Science & Technology* **2021**, *55*, Publisher: American Chemical Society, 9711–9720.

(25) World Bank Group *Global Gas Flaring Reduction Partnership: Gas Flaring Definitions*; tech. rep.; Washington, D.C.: World Bank Group, 2016.

(26) Tyner, D. R.; Johnson, M. R. A Techno-Economic Analysis of Methane Mitigation Potential from Reported Venting at Oil Production Sites in Alberta. *Environmental Science & Technology* **2018**, *52*, PMID: 30352509, 12877–12885.

(27) Allen, D. T.; Roman-White, S. A.; McCormick, M.; George, F. Moving toward Zero Routine Flaring in the Permian Basin Oil and Gas Production Region: Measuring Progress and Driving Factors. *ACS Sustainable Resource Management* **2024**, *1*, 1041–1046.

(28) Guanter, L. et al. Surveying methane point-source super-emissions across oil and gas basins with MethaneSAT. *Atmospheric Chemistry and Physics* **2026**, *26*, 2941–2963.

(29) East, J. D.; Jacob, D. J.; Jervis, D.; Balasus, N.; Estrada, L. A.; Hancock, S. E.; Sulprizio, M. P.; Thomas, J.; Wang, X.; Chen, Z.; Varon, D. J.; Worden, J. R. Worldwide inference of national methane emissions by inversion of satellite observations with UNFCCC prior estimates. *Nature Communications* **2025**, *16*, 11004.

(30) Elvidge, C. D.; Zhizhin, M.; Hsu, F. C.; Sparks, T.; Ghosh, T. Subpixel Analysis of Primary and Secondary Infrared Emitters with Nighttime VIIRS Data. *Fire* **2021**, *4*, 83.

(31) Elvidge, C. D.; Zhizhin, M.; Baugh, K.; Hsu, F. C.; Ghosh, T. Extending Nighttime Combustion Source Detection Limits with Short Wavelength VIIRS Data. *Remote Sensing* **2019**, *11*, 395.

(32) Liu, Y.; Hu, C.; Zhan, W.; Sun, C.; Murch, B.; Ma, L. Identifying industrial heat sources using time-series of the VIIRS Nightfire product with an object-oriented approach. *Remote Sensing of Environment* **2018**, *204*, 347–365.

(33) Zhizhin, M.; Matveev, A.; Ghosh, T.; Hsu, F.-C.; Howells, M.; Elvidge, C. Measuring Gas Flaring in Russia with Multispectral VIIRS Nightfire. *Remote Sensing* **2021**, *13*, Number: 16 Publisher: Multidisciplinary Digital Publishing Institute, 3078.

(34) Hu, C.; Zhang, X.; Xing, X.; Gao, Q. An approach to detect gas flaring sites using sentinel-2 MSI and NOAA-20 VIIRS images. *International Journal of Applied Earth Observation and Geoinformation* **2023**, *124*, 103534.

(35) Zhang, X.; Liu, L.; Chen, X.; Gao, Y.; Xie, S.; Mi, J. GLC_FCS30: global land-cover product with fine classification system at 30 m using time-series Landsat imagery. *Earth System Science Data* **2021**, *13*, 2753–2776.

(36) Omara, M.; Gautam, R.; O'Brien, M. A.; Himmelberger, A.; Franco, A.; Meisenhelder, K.; Hauser, G.; Lyon, D. R.; Chulakadabba, A.; Miller, C. C.; Franklin, J.; Wofsy, S. C.; Hamburg, S. P. Developing a spatially explicit global oil and gas infrastructure database for characterizing methane emission sources at high resolution. *Earth System Science Data* **2023**, *15*, Publisher: Copernicus GmbH, 3761–3790.

(37) Minet, L.; Azargoshasbi, F.; Franklin, M.; Schade, G. W.; McGregor, M. J.; McInnes, K.; Takaro, T. K. Analysis of Flaring Activity at Liquefied Natural Gas (LNG) Export Facilities Worldwide. *Environmental Science & Technology* **2025**, *59*, PMID: 40974299, 20357–20366.

(38) Franklin, M.; Chau, K.; Cushing, L. J.; Johnston, J. E. Characterizing Flaring from Unconventional Oil and Gas Operations in South Texas Using Satellite Observations. *Environmental Science & Technology* **2019**, *53*, PMID: 30657671, 2220–2228.

(39) Naus, S.; Maasakkers, J. D.; Gautam, R.; Omara, M.; Stikker, R.; Veenstra, A. K.; Nathan, B.; Irakulis-Loitxate, I.; Guanter, L.; Pandey, S.; Girard, M.; Lorente, A.; Borsdorff, T.; Aben, I. Assessing the Relative Importance of Satellite-Detected Methane Superemitters in Quantifying Total Emissions for Oil and Gas Production Areas in Algeria. *Environmental Science & Technology* **2023**, *57*, PMID: 37956986, 19545–19556.

(40) Irakulis-Loitxate, I.; Guanter, L.; Maasakkers, J. D.; Zavala-Araiza, D.; Aben, I. Satellites Detect Abatable Super-Emissions in One of the World's Largest Methane Hotspot Regions. *Environmental Science & Technology* **2022**, *56*, 2143–2152.

Supporting Information for

Satellite-based Assessment of Continuous and Episodic Flaring Regimes across Major Oil and Gas-producing Basins

Lulu Si[1,*], Shanyu Zhou[1], Debbie Walker[2], Itziar Irakulis-Loitxate[2], Javier Gorroño[1], Mark F. Lunt[3], and Luis Guanter[1]

[1]Research Institute of Water and Environmental Engineering (IIAMA), Universitat Politècnica de València (UPV), 46022. Valencia, Spain.
[2]International Methane Emission Observatory (IMEO), United Nations Environment Programme, 75015. Paris, France.
[3]Environmental Defense Fund, Perth, WA, Australia

*Email: lsi@doctor.upv.es

Number of pages: 18
Number of tables: 6
Number of figures: 15

S1 The indicators from upstream sector

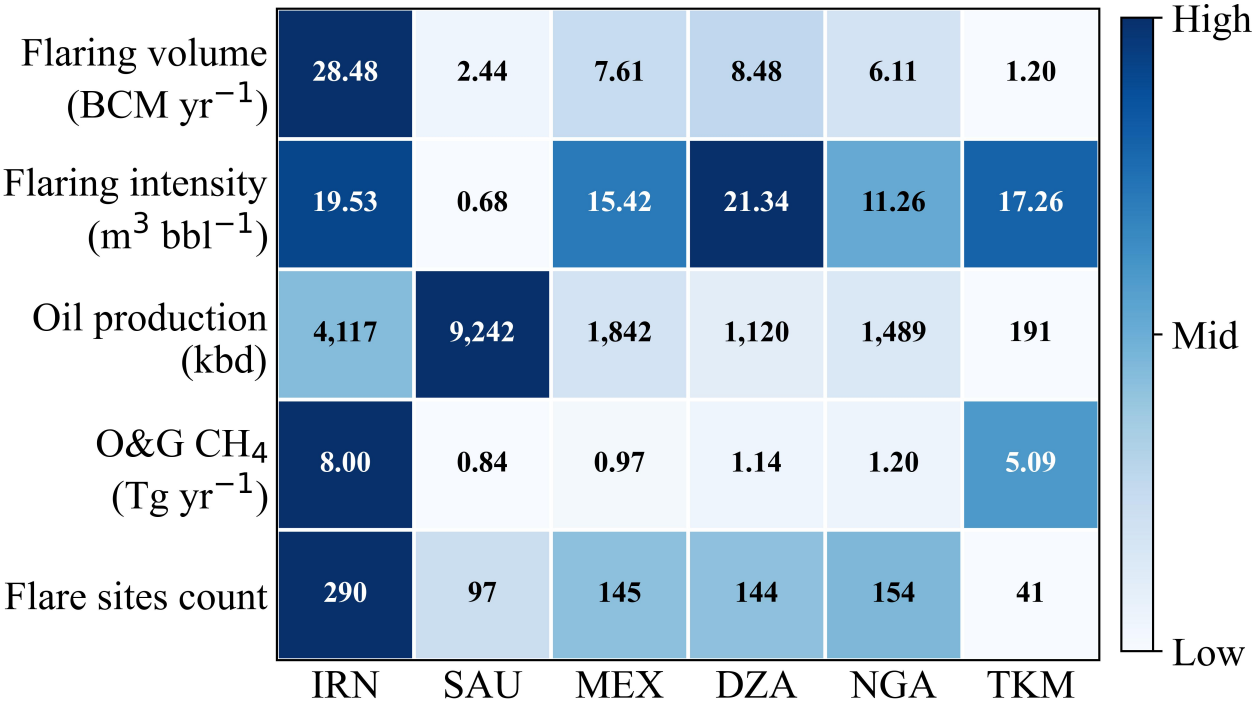


Figure S1: Key upstream indicators for each study country in 2024, including flaring volume, flaring intensity, oil production, flare sites count, and methane emissions. The first four indicators are from the World Bank Group (WBG) [1, 2], and the last indicator is from TROPOMI [3].

S2 Exploration of VIIRS data

(1) Timeseries records of VIIRS sites

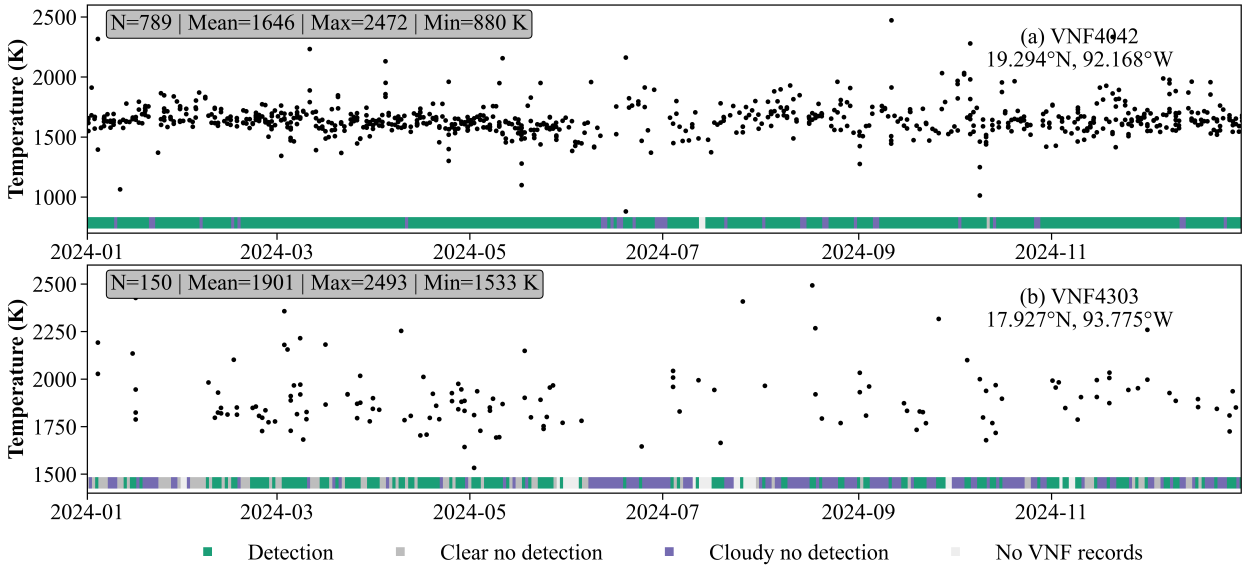


Figure S2: Representative time series of daily temperatures for two selected sites in 2024. Each point represents a valid daily temperature measurement. (a) Daily temperature time series for the site with VNF ID 4042, showing frequent observations and relatively persistent high-temperature activity. (b) Daily temperature time series for the site with VNF ID 4303, showing a more intermittent observation pattern. The summary statistics in each panel report the number of valid observations (N), mean temperature, maximum temperature, and minimum temperature. Site coordinates are shown in the upper-right corner of each panel.

(2) Data availability of VIIRS records

The data-count hierarchy summarizes the transition from the original WBG flare records to the VIIRS/EOG time-series sites used for rule-based classification. WBG records in 2024 represent the initial national flare inventory, whereas retained flare point records denote the matched WBG records that remained after applying oil, gas, and LNG upstream-source filters. The temporal classification was conducted at the VIIRS/EOG site level using IDMYC as link between mapped flare records and daily VNF observations. Because multiple flare records may correspond to the same IDMYC, the number of IDMYC-linked records can exceed the number of unique time-series data points. The resulting site-level class labels were then re-attributed to the retained flare-point records for spatial mapping and country-level summaries. This distinction is important for interpreting sample sizes. Inventory and mapping outputs are record based, whereas temporal classification outputs are site based. Small differences between the site with IDMYC and the final classified sites reflect the availability of usable VNF observations in 2024.

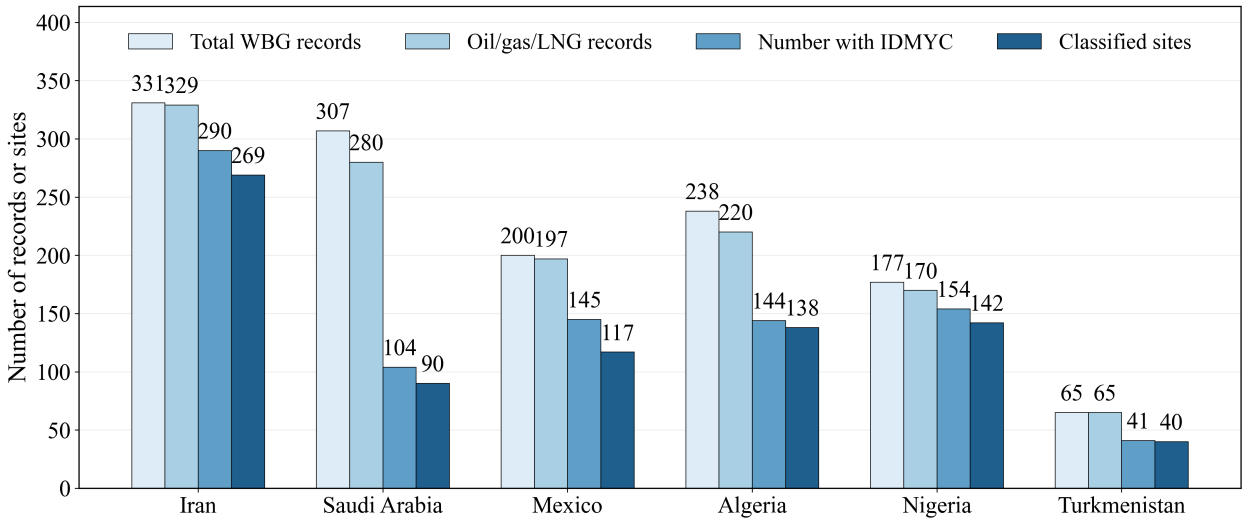


Figure S3: Data availability of VIIRS count in each investigated country.

S3 Flare site detection with Sentinel-2 and Landsat

Sentinel-2 MSI and Landsat 8/9 OLI observations were used to provide fine-scale spatial evidence for flare site identification and to complement the VIIRS site-level time-series analysis. The processing workflow consisted of three main stages: single-date thermal anomaly extraction, multi-temporal false positive filtering, and spatial matching with VIIRS flare sites (Fig. S4).

For each available cloud-free Sentinel or Landsat scene, shortwave-infrared (SWIR) bands were screened to identify high-temperature anomalies. The thermal anomaly index (TAI) was used to enhance the spectral contrast between high-temperature combustion sources and the surrounding background:

$$\mathrm{TAI} = \frac{\rho_{\lambda_2} - \rho_{\lambda_1}}{\rho_{\lambda_0}}, \tag{S1}$$

where ρ_λ denotes the top-of-atmosphere reflectance at wavelength λ. The subscripts λ_0, λ_1, and λ_2 correspond to the near-infrared (NIR), SWIR1, and SWIR2 bands, respectively. Sensor-specific band assignments used for TAI computation are listed in Table S1. Candidate flare pixels were then selected using TAI together with scene-adaptive SWIR thresholds, so that anomalous pixels were evaluated relative to the local radiance background instead of by a fixed global threshold. Saturated SWIR pixels and their immediate neighborhoods were also retained as potential flare candidates, because intense combustion sources may exceed the sensor radiometric range. Invalid observations affected by clouds, low-quality pixels, or unsuitable background conditions were removed before temporal aggregation.

Single-date detections were then aggregated across the observation period in 2024. Candidate flare locations were retained only when they showed repeated occurrences over time, thereby reducing transient false positives from cloud edges, sun glint, bright surfaces, or other artifacts. The retained candidates were spatially localized using sensor-specific procedures, including watershed-based localization for Sentinel data and buffer centroid localization for Landsat detection. Candidate sites were further evaluated using the corresponding VNF temperature records to confirm persistent high-temperature behavior. False positives from built-up surfaces were reduced using an impervious-surface mask derived from the GLC_FCS30 land-

Table S1: Spectral and spatial parameters used for thermal anomaly index (TAI) computation.

Sensor	**TAI term**	**Band**	λ_c **(nm)**	**Bandwidth (nm)**	**GSD (m)/ swath (km)**
Sentinel-2A MSI	λ_0 (NIR)	B8A	864.7	21	20 / 290
	λ_1 (SWIR1)	B11	1613.7	91	
	λ_2 (SWIR2)	B12	2202.4	175	
Sentinel-2B MSI	λ_0 (NIR)	B8A	864.0	22	20 / 290
	λ_1 (SWIR1)	B11	1610.4	94	
	λ_2 (SWIR2)	B12	2185.7	185	
Landsat 8/9 OLI	λ_0 (NIR)	B5	865.0	28	30 / 185
	λ_1 (SWIR1)	B6	1608.5	85	
	λ_2 (SWIR2)	B7	2200.5	187	

cover product [4].

The resulting Sentinel and Landsat flare detections were merged to form a unified high-spatial-resolution detection layer. These detections were then matched with VIIRS flare sites using a 1 km spatial search radius. For each VIIRS site, the number of matched high-resolution detections within the search radius was recorded. VIIRS sites with at least one matched high-resolution detection were treated as spatially confirmed, whereas unmatched VIIRS sites were retained as VIIRS-only records for subsequent interpretation. This matching preserves the complementary information provided by the two data sources: VIIRS supplies the temporally dense thermal record used for site-level activity classification, while Sentinel and Landsat provide a finer spatial localization and independent high-resolution evidence of combustion sources.

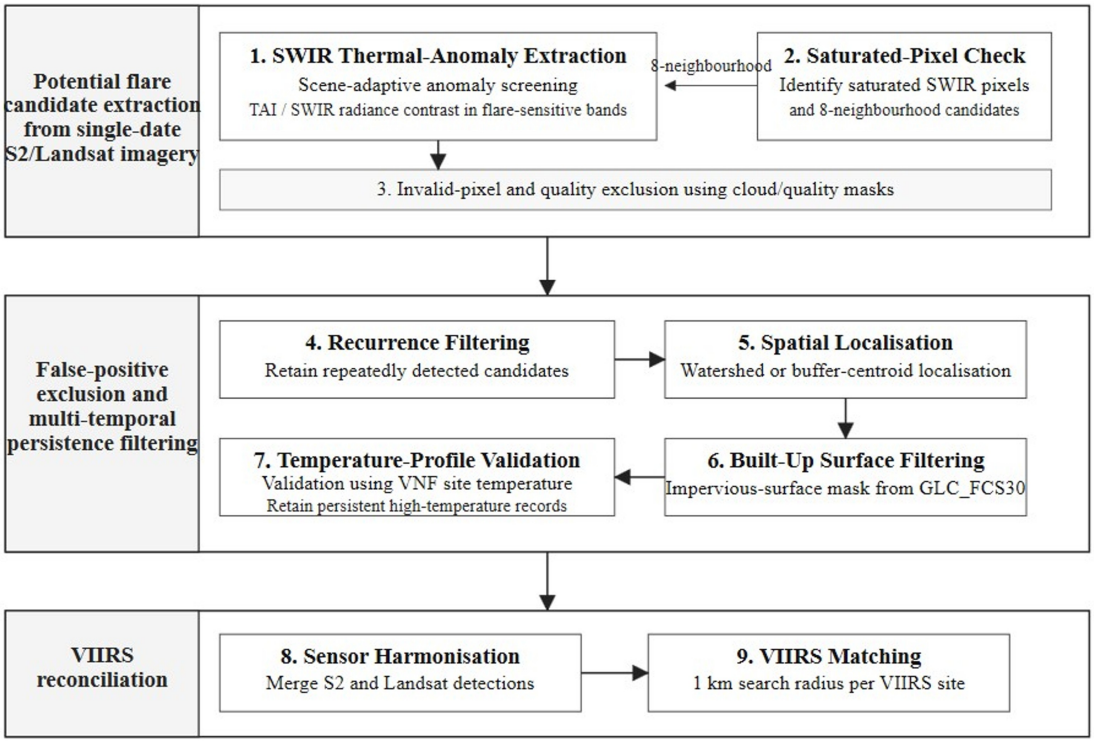


Figure S4: Workflow for high-spatial-resolution flare detection and matching with VIIRS flare sites [5, 6]. Sentinel-2 MSI and Landsat 8/9 OLI images were first screened for SWIR thermal anomalies using the thermal anomaly index, scene-adaptive thresholds, and saturated pixel checks. Candidate detections were filtered using image quality masks, multi-temporal recurrence, spatial localization, VNF site temperature validation, and built-up surface screening. The retained Sentinel and Landsat detections were then merged and matched to VIIRS flare sites using a 1 km search radius.

S4 OGIM Pipeline for gas recovery

The proximity analysis requires pipelines that can receive associated gas. We therefore classified OGIM pipelines by their reported commodity (Figure S5). OGIM records this attribute as free text compiled from multiple national sources. The same commodity is often reported under different names. For example, natural gas pipelines appear as gas, natural gas, sweet gas, sour gas and so on.

We grouped the original values into ten pipeline types. Four types carry natural gas that include gas, gas and NGL/LPG, gas and condensate, and mixed oil and gas. We defined these as gas-capable pipelines. They account for 51.6% of the total pipeline length and form the basis of the proximity analysis. Oil, condensate, NGL/LPG, refined products, and CO_2 pipelines cannot receive associated gas. We excluded them, together with pipelines carrying water or nitrogen. Excluded pipelines account for 33.6% of the total length.

Pipelines with an N/A commodity account for 14.8% of the total length. Their type cannot be determined from OGIM. We therefore did not use them in the proximity analysis.

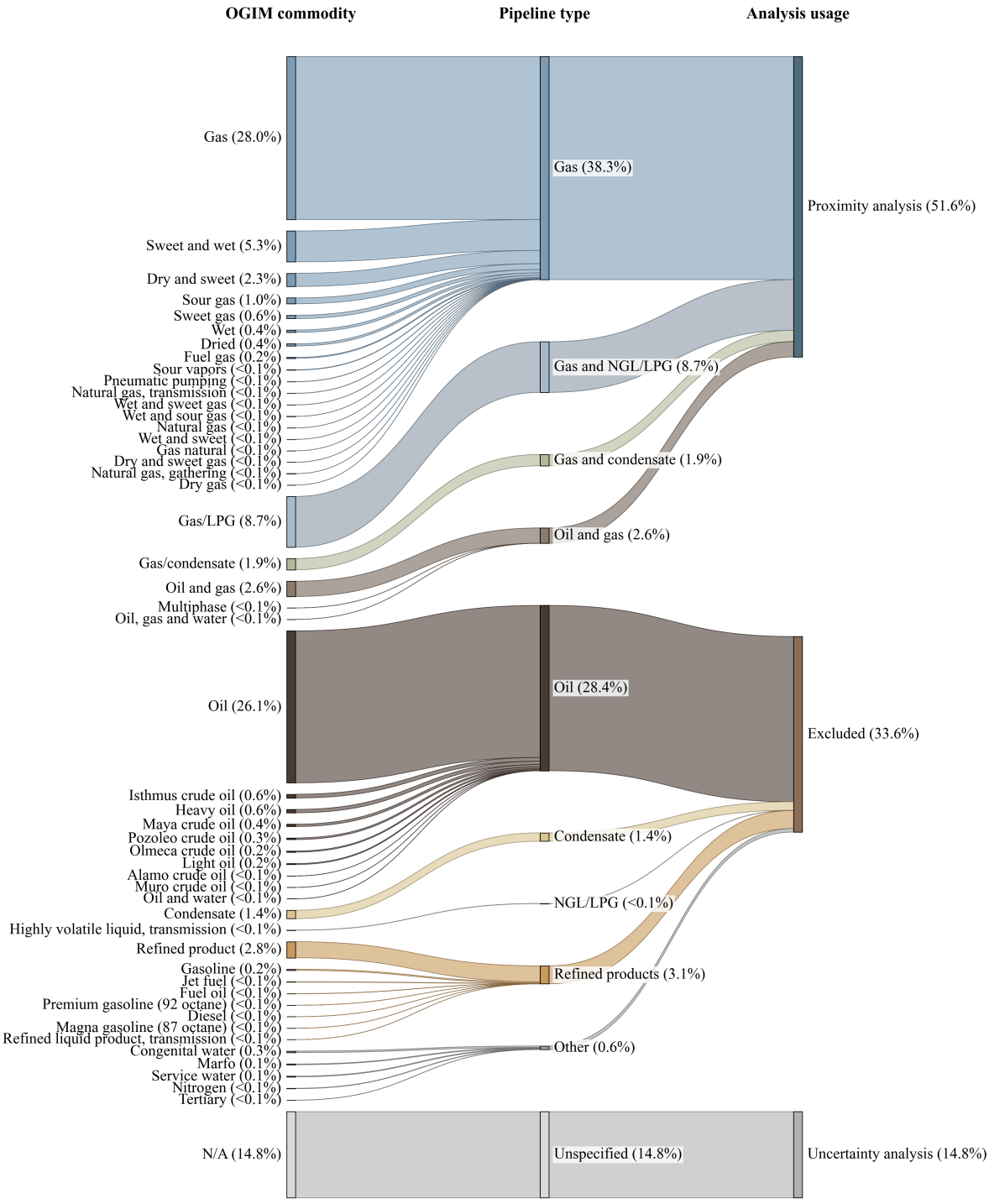


Figure S5: Classification of OGIM pipelines used in the pipeline proximity analysis. Flows are weighted by pipeline length and pooled across the six study countries. The left column shows the original commodity values reported in OGIM [7]. The middle column shows the pipeline types derived from these values. The right column shows how each pipeline type is used in the analysis. Percentages give the share of total pipeline length. Pipelines whose commodity includes natural gas are used in the proximity analysis. Pipelines with an N/A commodity are used only in the uncertainty analysis. All other pipelines are excluded.

S5 Classification of VIIRS sites

(1) Construction of cloud-adjusted temporal metrics

Cloud cover can affect the interpretation of temporal gaps in the daily VNF records. In the VNF product, non-detection records include a Cloud_Mask field that indicates whether the observation was clear, probably clear, probably cloudy, or cloudy. We used this field to distinguish clear-sky days without detections from cloudy days without detections before calculating the temporal metrics used for classification.

The activity ratio was calculated using valid VNF observation days as the denominator. Valid observation days were defined as detection days plus clear-sky non-detection days. Cloudy non-detection days and days without VNF records were excluded from the denominator. This gives the activity ratio:

$$\alpha = \frac{N_{\text{active}}}{N_{\text{valid}}}, \tag{S2}$$

where N_{active} is the number of active detection days and N_{valid} is the number of valid VNF observations in 2024.

Cloudy days without detections were also accounted for in the gap-related metrics. For each site, the activity ratio α was used as an empirical estimate of the probability that the site was active under otherwise unobserved cloudy conditions. Cloudy non-detection days were therefore downweighted by $(1 - \alpha)$ when calculating maximum gap duration and sparse monthly activity. This treatment considers cloudy days as uncertain observations rather than confirmed inactive days.

(2) Tier definitions and classification rule

Each metric was independently discretized into three tiers:

$$c = \begin{cases} \text{high} & \alpha \geq \tau_h \\ \text{mid} & \tau_l \leq \alpha < \tau_h \\ \text{low} & \alpha < \tau_l \end{cases} \qquad q = \begin{cases} \text{few} & g = 0 \\ \text{some} & 0 < g < \gamma \\ \text{many} & g \geq \gamma \end{cases} \tag{S3}$$

The joint pair (c, q) is mapped to a binary Continuous / Episodic label via the lookup table below (Table S2).

Table S2: Classification rule. Each cell gives the label assigned to the joint combination of continuity tier c (rows) and gap tier q (columns).

$c \setminus q$	**few**	**some**	**many**
high	Continuous	Continuous	Episodic
mid	Continuous	Episodic	Episodic
low	Episodic	Episodic	Episodic

(3) Empirical basis for temporal-threshold selection

The temporal thresholds used in rule-based classification were evaluated against the empirical distributions of site-level activity and interruption metrics. The activity ratio thresholds were set to $\tau_l = 0.40$ and $\tau_h = 0.84$, corresponding to approximately the 30th and 60th percentiles of the classified site-level activity

ratio distribution, respectively. Gap-related interruptions were represented using a secondary maximum-gap threshold of $\delta_m = 15$ days and a long-gap threshold of $\delta_l = 30$ days. The composite gap score threshold was set to $g = 2$ and the sparse-month threshold was set to $\theta_s = 2$.

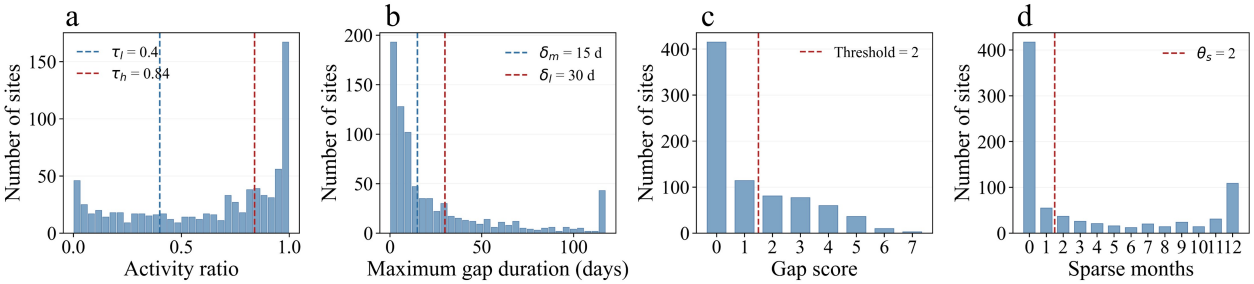


Figure S6: Empirical distributions of the temporal metrics used for the threshold-based classification. (a) Distribution of the activity ratio, with lower (τ_l)and upper (τ_h) continuity thresholds indicated by dashed lines. (b) Distribution of the maximum gap duration, with secondary (δ_m) and long-gap δ_l duration thresholds indicated. (c) Distribution of the composite gap score, with the threshold used to identify substantial temporal interruption. (d) Distribution of sparse-month counts, with the sparse-month threshold (θ_s) indicated.

Table S3: Threshold parameters used in the rule-based temporal classification.

Parameter	τ_h	τ_l	γ	δ_l	δ_m	θ_s	m_s
Value	0.84	0.40	2	30	15	2	10

(4) Rule table

The rule table summarizes how classified flare sites were distributed across the two temporal dimensions used in the rule-based classification framework. The first dimension describes the continuity of thermal activity, derived mainly from the annual activity ratio and related persistence metrics. The second dimension describes temporal interruption, represented by the frequency and magnitude of observation gaps. Combining these two dimensions provides a compact diagnostic view of site assignment within the rule-based decision space.

In the 3×3 rule table, the rows represent increasing levels of temporal continuity, whereas the columns represent increasing levels of temporal interruption. Each cell reports the number of sites that fall into the corresponding combination of continuity and gap categories for each country. Therefore, the table is used as a diagnostic summary of the classification process, showing whether the final classes are dominated by persistent, regularly observed sites or by sites with more intermittent temporal behavior.

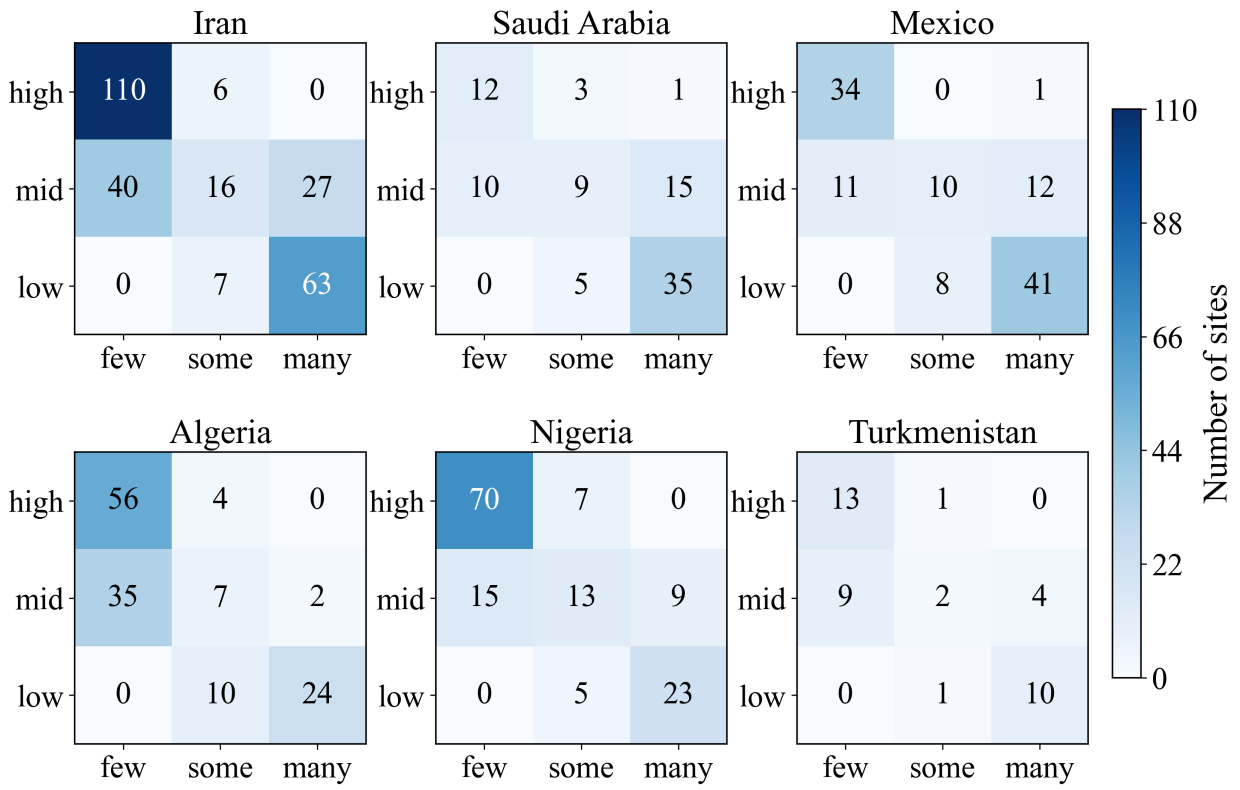


Figure S7: Distribution of classified flare sites per country displayed by 3 × 3 rule matrices. The rows represent continuity categories derived from temporal persistence metrics, and the columns represent gap categories derived from the frequency and magnitude of temporal interruptions. Cell values indicate the number of sites assigned to each continuity–gap combination.

S6 Cloud-related sensitivity in episodic classifications

We quantified cloudy no-detection days for sites classified as Episodic in 2024. The results show clear differences at the country level (Figure S8). At a 40% assessment threshold, 66% of episodic sites in Mexico and 86% in Nigeria had cloudy no-detection days above this level. The corresponding fractions were 17% in Turkmenistan and 0% in Iran, Saudi Arabia, and Algeria. These results indicate that episodic classifications in Mexico and Nigeria have a higher cloud-related uncertainty, because temporal gaps in these countries are more likely to include cloud-obscured non-detections.

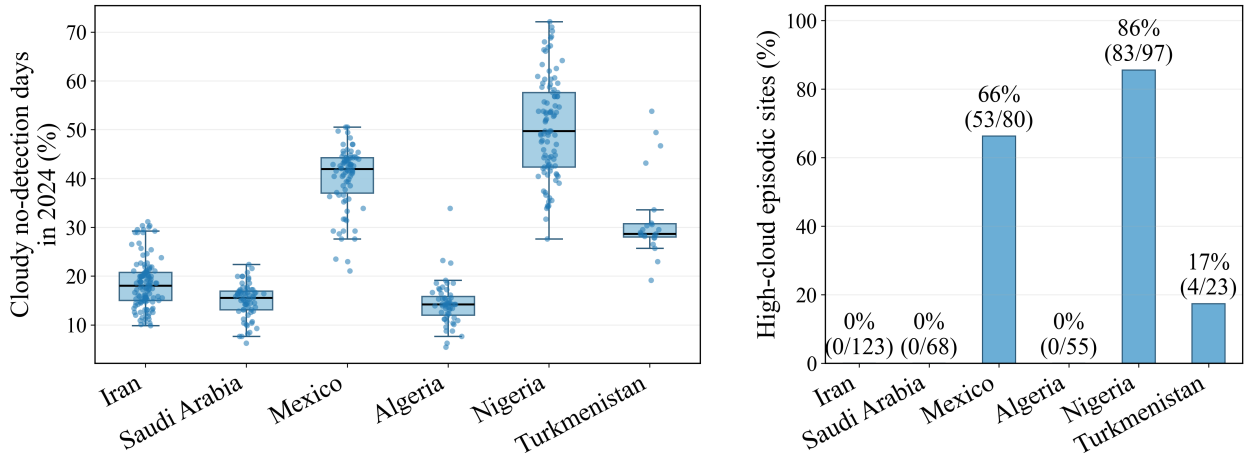


Figure S8: Cloud-related uncertainty assessment for sites classified as Episodic in 2024. (a) Fraction of cloudy no-detection days for episodic sites by country. (b) Percentage of episodic sites in each country with cloudy no-detection days greater than or equal to 40% in 2024.

To further evaluate how cloudy days could affect the temporal classification, we examined the distribution of cloudy fractions together with two bounding sensitivity scenarios (Figure S9). In the first scenario, cloudy observations were removed from the temporal sequence and treated as unavailable observations. The second scenario treated cloudy days as potential active days, representing an upper bound assumption for hidden flare activity under cloudy conditions.

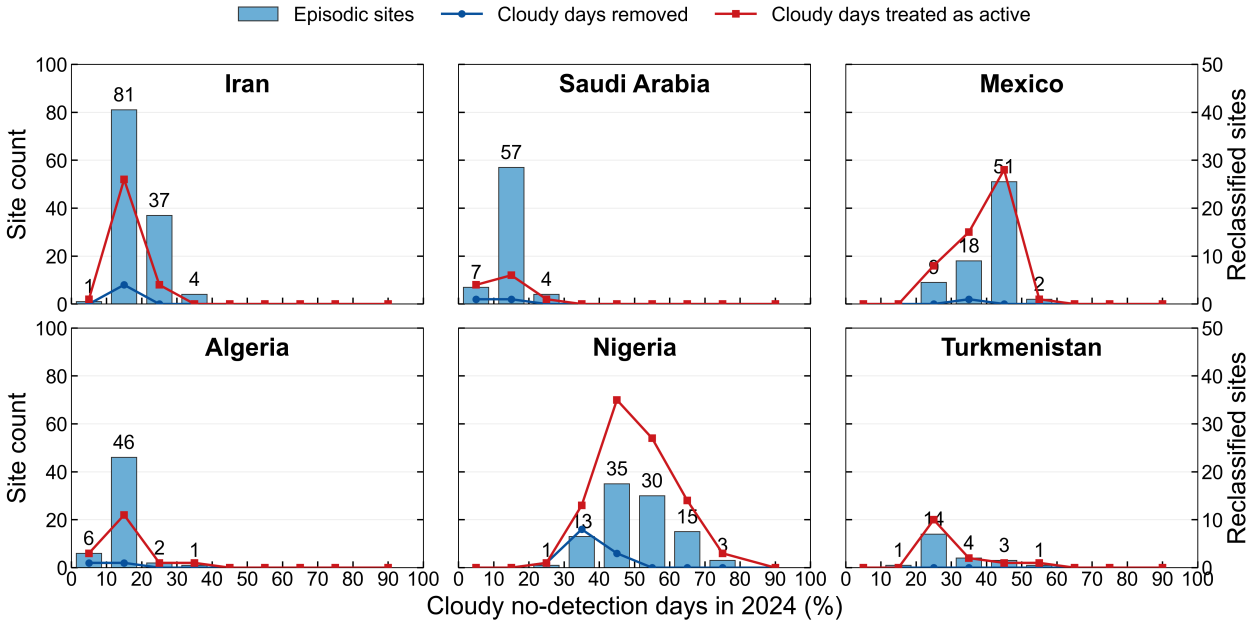


Figure S9: The count distribution of cloudy obervations and extreme sensitivity by each investigated country for sites classified as Episodic in 2024. Bars show the number of Episodic sites in each cloudy fraction. Blue lines show the number of sites that would change from Episodic to Continuous if cloudy days were removed from the temporal sequence. Red lines show the number of sites that would change from Episodic to Continuous if cloudy days were treated as active days.

Table S4 reports the number of sites originally classified as Episodic that would change to Continuous after the sensitivity analysis. When cloudy days without measurements were excluded from temporal gap calculations, the resulting changes were limited in most countries. The proportion of Episodic sites reclassified as Continuous amount to 8.1% in Iran, 4.4% in Saudi Arabia, 10.0% in Mexico, 21.8% in Algeria, and 26.1% in Turkmenistan. Nigeria showed a larger response, with 48.5% of Episodic sites reclassified as Continuous. These results indicate that a cloud related uncertainty is most relevant for Episodic classifications in countries with frequent cloudiness and resulting limitations. Cloudy days without the possibility of measurements do not provide direct evidence of flare activity.

Table S4: Episodic sites counts before and after excluding days under cloudy condition.

Country	**Episodic sites**	**Reclassified sites**	**Reclassified sites (%)**
Iran	123	10	8.1
Nigeria	97	47	48.5
Mexico	80	8	10.0
Saudi Arabia	68	3	4.4
Algeria	55	12	21.8
Turkmenistan	23	6	26.1

S7 Summary of VIIRS classification results

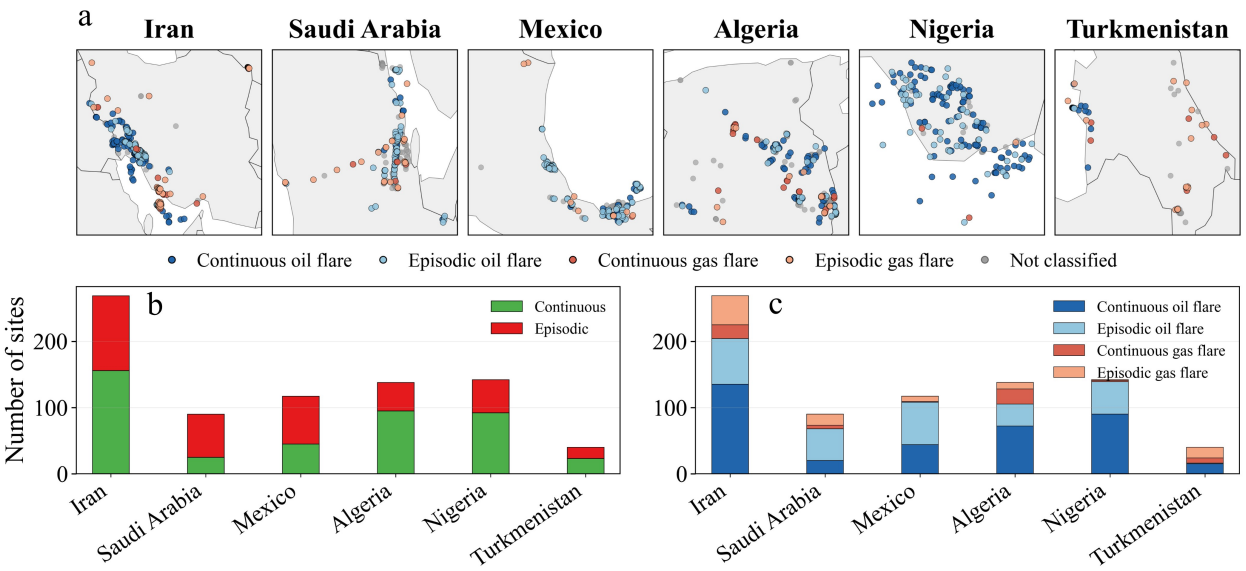


Figure S10: Summary of VIIRS flare classification results derived from the rule-based temporal classification framework for all country investigated. (a) Spatial distribution of all VIIRS flare sites in each country. (b) Number of sites classified as continuous or episodic according to temporal persistence and gap-structure criteria. (c) Number of sites grouped into fuel-specific operational classes by combining temporal behavior with oil/gas attribution.

S8 Robustness evaluation

The robustness of the rule-based classification was evaluated by comparing its site-type labels with those obtained from alternative unsupervised and semi-supervised methods. All comparisons were conducted using the common set of sites for which both the rule-based and alternative labels were available. Four complementary agreement metrics were used: Overall Agreement, Cohen's κ, Adjusted Rand Index (ARI), and Normalized Mutual Information (NMI) [8–10].

The Overall Agreement was calculated as the proportion of sites assigned to the same class by rule-based and alternative methods:

$$\text{Agreement} = \frac{1}{N}\sum_{i=1}^{N} I(y_i^{\text{rule}} = y_i^{\text{alt}}),$$

where N is the number of common sites, y_i^{rule} and y_i^{alt} are the labels assigned by the rule-based and alternative methods, respectively, and $I(\cdot)$ is an indicator function. Cohen's κ was used to account for the level of agreement expected by chance. The ARI measures the similarity between two label partitions after correcting for random agreement, while the NMI quantifies the shared information between the two classifications after normalization. ARI and NMI were computed using standard implementations in `scikit-learn`.

The semi-supervised methods showed very high consistency with the rule-based labels, with agreement exceeding 99% and Cohen's κ greater than 0.98. This indicates that the rule-based classification is consistent with data-driven labels when partial label information is available. In contrast, the two unsupervised clustering methods showed lower agreement. K-means retained moderate agreement, whereas hierarchical clustering showed the weakest consistency. This difference indicates that purely distance-based clustering is sensitive to the structure of the temporal feature space and does not fully reproduce the persistence and gap criteria used in the rule-based classification. Therefore, the robustness assessment supports the interpretability of the rule-based framework. It also showing that unsupervised clustering alone is not an adequate substitute for the operational classification rules.

Table S5: Comparison of the robustness between the rule-based classification and alternative methods.

Method	N	Agreement (%)	Cohen's κ	ARI	NMI
Label propagation	796	99.372	0.987	0.975	0.951
Self-training	796	99.372	0.987	0.975	0.946
K-means	796	79.523	0.604	0.347	0.423
Hierarchical	796	67.337	0.386	0.116	0.265

Note: N denotes the number of common sites compared between the rule-based classification and each alternative method.

S9 Flare count matching and comparison

(1) Flare data matching

Spatial matching between VIIRS flare sites and high-spatial-resolution flare candidates was performed using a fixed buffer radius around each VIIRS site. To evaluate the influence of this distance threshold, we first tested how the match rate changed across a range of buffer radii (Fig. S11). Sensitivity analysis supports the use of a matching radius of 1 km, which provides a balance between preserving matched detections and limiting excessive spatial aggregation.

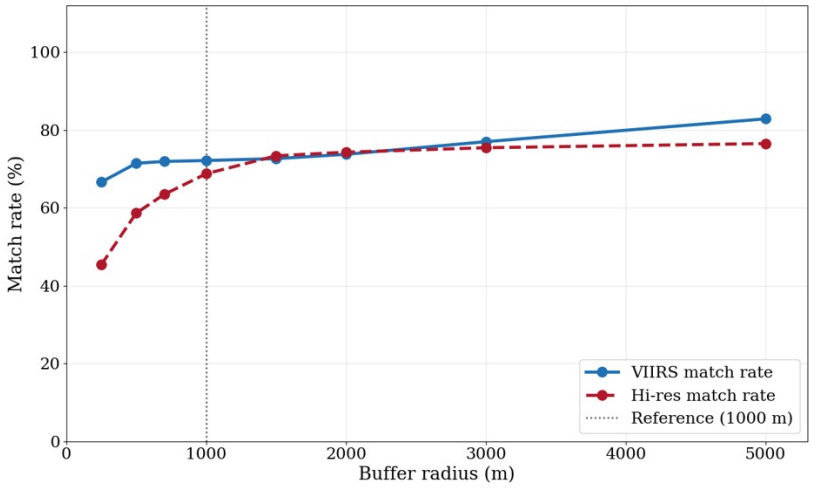


Figure S11: Sensitivity of spatial matching between VIIRS flare sites and high-spatial-resolution flare candidates to varying buffer radii. The blue line shows the proportion of VIIRS flare sites associated with at least one high-spatial-resolution candidate, whereas the red dashed line indicates the proportion of high-spatial-resolution candidates associated with a VIIRS site. The vertical dotted line marks the 1000 m reference buffer used for the matching analysis. Match rates increase rapidly at short distances and show reduced marginal gains around the reference threshold, suggesting that the 1000 m buffer provides a stable compromise between matching completeness and spatial specificity.

(2) Flare count comparison

A comparison between the VIIRS flare sites and high-spatial-resolution flare detections provided an overview of the relative inventory size derived from the two observation scales. VIIRS represents the flare activity at the site level, whereas Sentinel and Landsat detections provide a finer spatial localization of individual high-temperature sources. Therefore, a count comparison is used to summarize the country-level correspondence of the VIIRS-based inventory and the high-spatial-resolution detection layer.

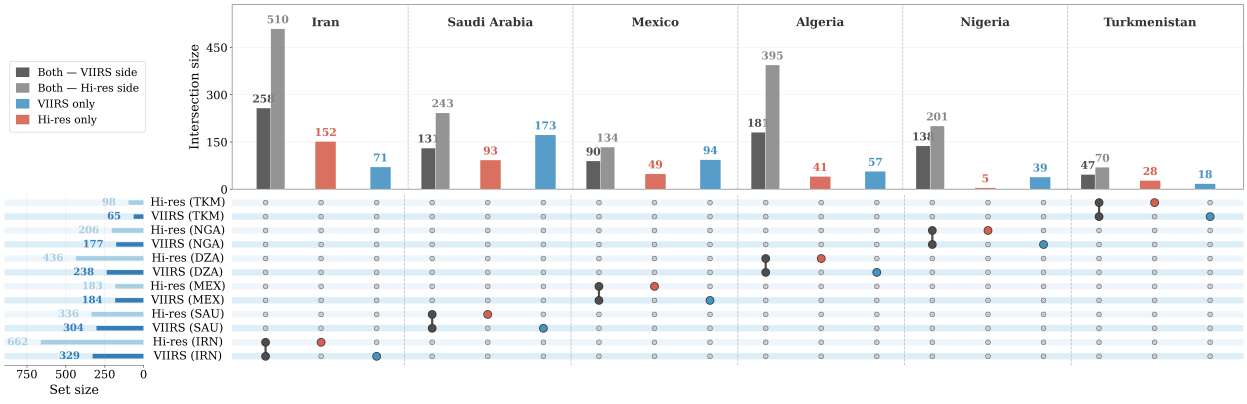


Figure S12: Count comparison between VIIRS flare sites and high-spatial-resolution flare detections for each country investigated. The figure summarizes the number of VIIRS sites and Sentinel/Landsat detections considered in the matching analysis for each country, providing an overview of the relative inventory size across observation scales.

S10 Abbreviation of basin names

Table S6: Basin names and abbreviations used in the basin-level analysis [7].

Country	No.	Basin name	Abbrev.
Algeria	1	ILLIZI–GHADAMES	ILG
Algeria	2	OUED MYA	OUM
Algeria	3	SAHARA	SAH
Algeria	4	ATLAS	ATL
Algeria	5	GOURARA	GOU
Iran	1	ZAGROS FOLDBELT	ZAF
Iran	2	CENTRAL IRAN–KAVIR	CIK
Iran	3	WIDYAN–NORTH ARABIAN GULF	WNA
Iran	4	RUB AL KHALI	RAK
Iran	5	AMU-DAR'YA	AMU
Iran	6	SOUTH CASPIAN	SOC
Mexico	1	MACUSPANA	MAC
Mexico	2	ISTHMUS SALINE	ISS
Mexico	3	SABINAS	SAB
Mexico	4	TAMPICO-MISANTLA-MAGISCAT	TAM
Mexico	5	COMALCALCO	COM
Mexico	6	VERACRUZ	VER
Mexico	7	BURGOS	BUR
Nigeria	1	NIGER DELTA	NID
Nigeria	2	BENUE TROUGH	BET
Nigeria	3	KETA–TOGO–BENIN	KTB
Saudi Arabia	1	WIDYAN–NORTH ARABIAN GULF	WNA
Saudi Arabia	2	RED SEA	RES
Saudi Arabia	3	RUB AL KHALI	RAK
Turkmenistan	1	AMU-DAR'YA	AMU
Turkmenistan	2	SOUTH CASPIAN	SOC
Turkmenistan	3	NORTH CAUCASUS	NOC
Turkmenistan	4	MANGYSHLAK–USTYURT	MAU

S11 Area-source methane detection with MethaneSAT

MethaneSAT area-source retrievals were used as an additional spatial context for interpreting the relationship between classified flare sites and regional methane emission patterns. Unlike point-source plume catalogues, MethaneSAT provides gridded methane flux estimates over broader source regions, allowing flare classes to be compared with spatially continuous methane emission fields.

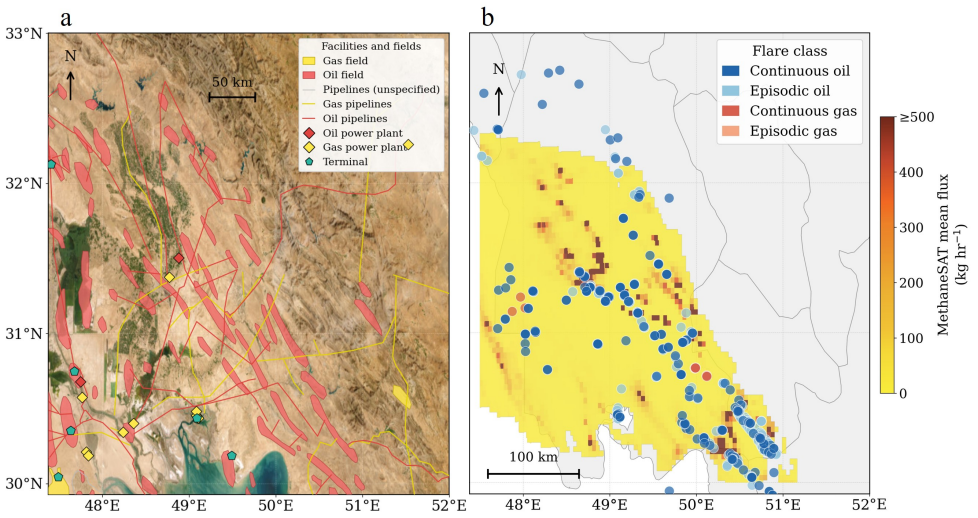


Figure S13: Oil and gas infrastructure, classified flare sites, and MethaneSAT area-source methane flux in Iran. (a) Oil and gas fields classified by reservoir type (oil or gas), together with oil and gas pipelines, petroleum terminals, and natural gas compressor stations from the Oil and Gas Infrastructure Mapping (OGIM) database [7]. Background satellite image from ESRI. (b) Example of spatial overlap between classified flare sites and MethaneSAT area-source methane flux estimates. The raster layer shows MethaneSAT mean methane flux in kg hr^{-1}, with warmer colors indicating higher flux values. The points indicate classified flare sites, separated into continuous oil, episodic oil, continuous gas, and episodic gas classes. This example shows that classified flare sites, particularly continuous oil flares, are spatially concentrated within or near MethaneSAT high-flux areas, providing areal source context for interpreting whether methane enhancements are co-located with persistent flaring activity.

S12 Matched flare volume and flux rate of methane plume

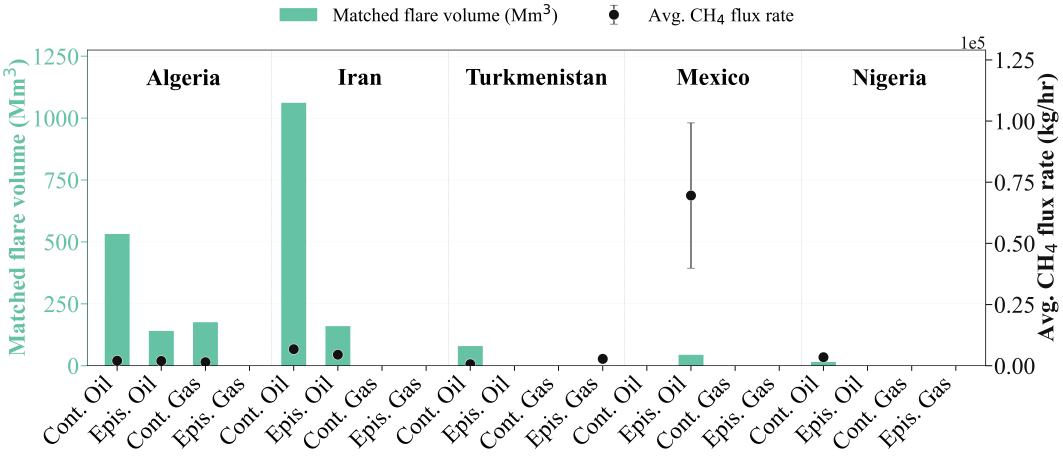


Figure S14: Class-resolved flare volume and methane flux rate for flare sites co-located with methane plume. Bars show the corresponding VIIRS flare volumes (Mm^3) associated with flare sites matched to methane plume detections, aggregated by country and the operational flare class. Points with error bars indicate the mean and standard deviation of methane flux rates (kg hr^{-1}) for matched IMEO and Carbon Mapper detections. This figure provides a supplementary volumetric and emission rate context for evaluating which flare classes are most strongly associated with satellite-observed increases in methane levels.

S13 Pipeline commodity composition by country

The pipeline proximity analysis used only gas-capable pipelines (Section S4). Figure S15 shows the commodity composition of OGIM pipelines in each country. The composition differs markedly across countries. Gas-capable pipelines dominate in Algeria (65.4%), Mexico (69.4%), and Iran (57.4%). In Algeria, most of this length is reported as gas/LPG pipelines. Saudi Arabia shows the opposite pattern. Oil/liquid pipelines account for 67.4% of its network, and gas-capable pipelines for only 23.2%. Nigeria has a mixed pipeline of gas and condensate (34.5%), oil (30.0%), and refined product (35.5%) pipelines. The share of pipelines without valid commodity records also varies. It is highest in Turkmenistan (38.9%) and Mexico (18.6%), and below 11% in Iran and Saudi Arabia. Algeria and Nigeria report a commodity for all pipelines. For countries with a large N/A share, the proximity analysis may underestimate the number of flare sites near gas pipelines.

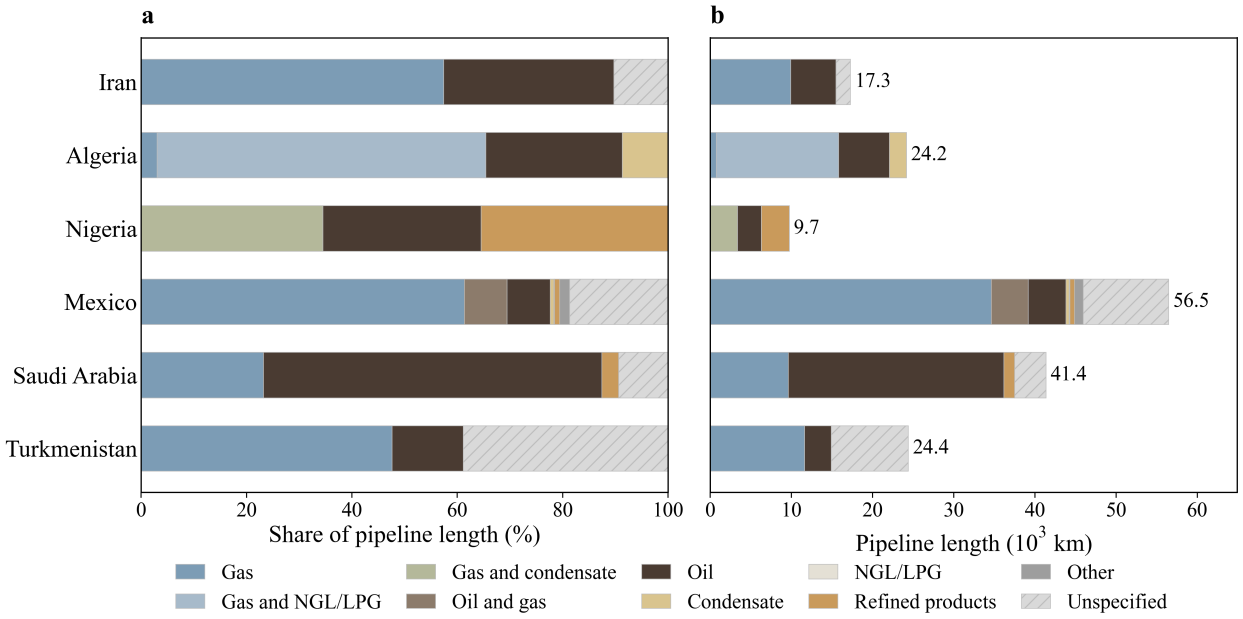


Figure S15: Commodity composition of OGIM pipelines in the six investigated countries. (a) Share of total pipeline length by pipeline type. (b) Pipeline length by type. Countries are ordered as in Figure 5.

References

(1) Zhizhin, M.; Elvidge, C. D.; Sparks, T.; Ghosh, T.; Bazilian, M.; Hsu, F.-C. An Improved Calibration for Satellite Estimation of Flared Gas Volumes from VIIRS Nighttime Data. *Energies* **2025**, *18*, Publisher: Multidisciplinary Digital Publishing Institute.

(2) About GFMR, World Bank `https://www.worldbank.org/en/programs/gasflaringreduction/about` (accessed 06/16/2026).

(3) East, J. D.; Jacob, D. J.; Jervis, D.; Balasus, N.; Estrada, L. A.; Hancock, S. E.; Sulprizio, M. P.; Thomas, J.; Wang, X.; Chen, Z.; Varon, D. J.; Worden, J. R. Worldwide inference of national methane emissions by inversion of satellite observations with UNFCCC prior estimates. *Nature Communications* **2025**, *16*, 11004.

(4) Zhang, X.; Zhao, T.; Xu, H.; Liu, W.; Wang, J.; Chen, X.; Liu, L. GLC_FCS30D: the first global 30 m land-cover dynamics monitoring product with a fine classification system for the period from 1985 to 2022 generated using dense-time-series Landsat imagery and the continuous change-detection method. *Earth System Science Data* **2024**, *16*, 1353–1381.

(5) Hu, C.; Zhang, X.; Xing, X.; Gao, Q. An approach to detect gas flaring sites using sentinel-2 MSI and NOAA-20 VIIRS images. *International Journal of Applied Earth Observation and Geoinformation* **2023**, *124*, 103534.

(6) Elvidge, C. D.; Zhizhin, M.; Hsu, F. C.; Sparks, T.; Ghosh, T. Subpixel Analysis of Primary and Secondary Infrared Emitters with Nighttime VIIRS Data. *Fire* **2021**, *4*, 83.

(7) Omara, M.; Gautam, R.; O'Brien, M. A.; Himmelberger, A.; Franco, A.; Meisenhelder, K.; Hauser, G.; Lyon, D. R.; Chulakadabba, A.; Miller, C. C.; Franklin, J.; Wofsy, S. C.; Hamburg, S. P. Developing a spatially explicit global oil and gas infrastructure database for characterizing methane emission sources at high resolution. *Earth System Science Data* **2023**, *15*, Publisher: Copernicus GmbH, 3761–3790.

(8) Wang, J.; Yang, Y.; Xia, B. A Simplified Cohen's Kappa for Use in Binary Classification Data Annotation Tasks. *IEEE Access* **2019**, *7*, 164386–164397.

(9) Zhang, S.; Wong, H.-S.; Shen, Y. Generalized Adjusted Rand Indices for cluster ensembles. *Pattern Recognition* **2012**, *45*, Brain Decoding, 2214–2226.

(10) Estevez, P. A.; Tesmer, M.; Perez, C. A.; Zurada, J. M. Normalized Mutual Information Feature Selection. *IEEE Transactions on Neural Networks* **2009**, *20*, 189–201.